

Palladium and silver abundances in stars with $[\text{Fe}/\text{H}] > -2.6$

Xiaoshu Wu^{1,2,3}, Liang Wang¹, Jianrong Shi¹, Gang Zhao¹, and Frank Grupp³

¹ Key Laboratory of Optical Astronomy, National Astronomical Observatories, Chinese Academy of Sciences, A20, Datun Road, Chaoyang District, Beijing 100012, China
e-mail: xswu@nao.cas.cn; gzhao@nao.cas.cn

² University of the Chinese Academy of Sciences, 19A, Yuquan Road, Shijingshan District, Beijing 100049, China

³ Max-Planck-Institut für Extraterrestrische Physik, Giessenbachstrasse, D-85748 Garching, Germany

Received; accepted

ABSTRACT

Palladium (Pd) and silver (Ag) are the key elements for probing the weak component in the rapid neutron-capture process (*r*-process) of stellar nucleosynthesis. We performed a detailed analysis of the high-resolution and high signal-to-noise ratio near-UV spectra from the archive of HIRES on the Keck telescope, UVES on the VLT, and HDS on the Subaru Telescope, to determine the Pd and Ag abundances of 95 stars. This sample covers a wide metallicity range with $-2.6 \lesssim [\text{Fe}/\text{H}] \lesssim +0.1$, and most of them are dwarfs. The plane-parallel LTE MAFAGS-OS model atmosphere was adopted, and the spectral synthesis method was used to derive the Pd and Ag abundances from Pd I λ 3404 Å and Ag I λ 3280/3382 Å lines. We found that both elements are enhanced in metal-poor stars, and their ratios to iron show flat trends at $-0.6 < [\text{Fe}/\text{H}] < +0.1$. The abundance ratios of [Ag/H] and [Pd/H] are well correlated over the whole abundance range. This implies that Pd and Ag have similar formation mechanisms during the Galactic evolution.

Key words. stars: abundances – stars: Population II – Galaxy: evolution

1. Introduction

More than half a century ago, forerunners established the theoretical framework for exploring the nucleosynthesis mechanisms. The nuclides with $Z > 30$ are produced by neutron-capture process (Cameron 1957; Burbidge et al. 1957), including at least two different dominant processes – the rapid one and the slow one. The slow neutron-capture nucleosynthesis process (*s*-process) accounts for the production of around half of the nuclear species beyond the iron-peak elements and takes place in a relatively low neutron density environment (Käppeler et al. 1989; Zhao & Magain 1990; Busso et al. 1999; Käppeler et al. 2011), whereas the rapid neutron-capture process (*r*-process) is responsible for the other half and occurs in a high neutron density environment (Kratz et al. 2007; Sneden et al. 2008; Farouqi et al. 2009, 2010). Besides, the lighter element primary process (LEPP; Travaglio et al. 2004; Montes et al. 2007; Arcones & Montes 2011) and the *p*-process (Arnould & Goriely 2003) are also thought to contribute to the overall stellar abundance patterns. As a result, the *r*-process always arises in explosive environments that can offer enough dense neutrons, such as neutron star mergers (Freiburghaus et al. 1999; Rosswog et al. 1999; Goriely et al. 2005, 2011; Korobkin et al. 2012; Perego et al. 2014; Just et al. 2015), neutrino-driven wind (Woosley et al. 1997; Arcones & Montes 2011; Wanajo & Janka 2012), jets in core-collapse supernova (Cameron 2001), massive core-collapse supernova (Wasserburg & Qian 2000; Argast et al. 2004), gamma-ray bursts (McLaughlin & Surman 2005), and low-mass supernova explosion from the collapse in O-Ne-Mg cores (Wanajo et al. 2003).

In contrast to this, the *s*-process happens in relatively peaceful environments. Much research has shown that the *s*-process

can be classified into two subprocesses. The main *s*-process, which happens in asymptotic giant branch (AGB) stars with masses between 1.3 and 8 M_{\odot} , creates the heavier elements, such as Ba (e.g., Straniero et al. 1997; Gallino et al. 1998; Busso et al. 1999; Karakas et al. 2009; Cristallo et al. 2009; Bisterzo et al. 2010), while the weak *s*-process is associated with massive stars with initial mass $> 8 M_{\odot}$, and it creates the lighter elements, such as Sr (Pignatari et al. 2010, 2013; Frischknecht et al. 2012). In addition, a third sub-*s*-process, the “strong” component, was proposed to explain about 50% of ^{208}Pb in the Sun (Clayton & Rassbach 1967) but was later re-interpreted as the outcome of the main *s*-process at low metallicity (Gallino et al. 1998; Travaglio et al. 2001).

Although several scenarios may be responsible for the *r*-process, their sites remain unclear. Observations suggest that the *r*-process can be divided into two distinct components, namely the main *r*-process and the weak *r*-process (e.g., Burris et al. 2000; François et al. 2007; Hansen & Primas 2011). Among the elements with $38 < Z < 50$, Pd and Ag are considered as the keys to an investigation of the weak *r*-process. Crawford et al. (1998) reported the first detection of Ag abundances in four metal-poor stars and found that $\langle [\text{Ag}/\text{Fe}] \rangle \simeq 0.22$ dex without any trend with [Fe/H]. Johnson & Bolte (2002) determined Pd and Ag abundances for three metal-poor stars and upper limits of Pd for another nine stars, but their correlation is not well established owing to the very small number of samples. Other studies gave Pd or Ag abundances for a few isolated metal-poor stars, e.g., CS 31082-001 (Hill et al. 2002), CS 22892-052 (Sneden et al. 2003), and HD 122563 (Honda et al. 2006).

It was not until Hansen & Primas (2011) and Hansen et al. (2012) that Pd and Ag abundances were analyzed for a large sample of stars. These authors derived Pd and Ag abundances for 34 dwarfs and 23 giants. The [Pd/Fe] and [Ag/Fe] show flat

Send offprint requests to: G. Zhao; e-mail: gzhao@nao.cas.cn

trends with metallicity and were compared with several tracer elements such as Sr, Y, Zr, Ba, and Eu. The comparisons have ruled out the weak/main *s*-process or main *r*-process as the main formation channels of Pd and Ag.

To study the formation processes of Pd and Ag further in the Galactic chemical evolution history, we analyzed the archive near-UV spectra for a large sample of stars, from three 8-10m class telescopes. These samples cover a wide metallicity range ($-3.1 \lesssim [\text{Fe}/\text{H}] \lesssim +0.1$) and represent different Galactic populations (thin disk, thick disk, halo). This paper is organized as follows. Section 2 describes the observations and data reduction; section 3 explains the atmosphere models, stellar parameters, and atomic data; section 4 gives the chemical abundance and error estimations; and the results are discussed in section 5. In the last section, we summarize our work and present conclusions.

2. Observation and data reduction

We searched the archive data of the High Resolution Echelle Spectrometer (HIRES; Vogt et al. 1994) attached to the Keck I Telescope to find the high-resolution ultraviolet spectral observations covering the wavelengths of $3200 \text{ \AA} \leq \lambda \leq 3500 \text{ \AA}$, where Pd I and Ag I lines might exist. We found 134 stars, of which spectra with high signal-to-noise ratios (S/N) are available from Keck I/HIRES. Most of these spectra were taken in the same project as the one that aims to determine beryllium abundances with the Be resonance doublet at $\lambda 3130.4/3131.1 \text{ \AA}$ (Boesgaard et al. 2011). The typical S/N is above 100 for the Ag I region and above 120 for the Pd I region. In addition, these spectra have been taken with the same instrumental configuration, and the wavelength resolving power ($\lambda/\Delta\lambda$) is $\sim 48\,000$. The data reduction was performed using the IRAF¹ ECHELLE software package, following the standard procedure including bias correction, flat fielding, background subtraction, and wavelength calibration. Whenever possible, one-dimensional spectra of several continuous frames for the same star were co-added to obtain a higher S/N and to remove the cosmic-ray hints. The continuum were normalized with polynomials, and the radial velocities were corrected by finding the maximum of their cross-correlation functions with the solar spectra. Of the 134 stars, about half (60 stars) have detectable Pd I line at $\lambda 3404.5 \text{ \AA}$ or Ag I resonance doublet at $\lambda 3280.7/3382.9 \text{ \AA}$, all of which are main-sequence or slightly-evolved stars, with effective temperatures (T_{eff}) ranging from 5000 K to 6350 K and metallicities ranging from $[\text{Fe}/\text{H}] = -2.6$ to 0.05.

To enlarge our sample, we searched the archive data of the High Dispersion Spectrograph further (HDS; Noguchi et al. 2002), which is mounted on the 8.2m Subaru Telescope. We selected seven stars with high S/Ns and clear Pd I or Ag I lines in the same wavelength region. All of the stars were observed with StdUb setting and the resolving power is $\sim 50,000$, comparable to that of HIRES sample. We reduced their spectra in the same manner as we used with Keck/HIRES data. This subsample covers a wide metallicity range ($-2.63 \leq [\text{Fe}/\text{H}] \leq 0.02$) and contains two metal-poor giants (HD 6268 and HD 110184).

In addition, we selected high S/N spectra of 28 stars taken with the Ultraviolet and Visual Echelle Spectrograph (UVES; Dekker et al. 2000) at ESO VLT 8.2m Kueyen telescope. 25 of them were obtained from the ESO Science Archive, and

¹ IRAF is distributed by National Optical Astronomy Observatories, operated by the Association of Universities for Research in Astronomy, Inc., under contract with the National Science Foundation, USA.

the remaining three were taken from the UVES-POP survey (Bagnulo et al. 2003). This subsample was analyzed in previous research on Be abundances (Tan et al. 2009), ensuring a large overlap with the dwarf sample of Hansen & Primas (2011) and Hansen et al. (2012), which enables us to make a direct comparison of our results with the previous studies. These spectra were reduced using the ESO MIDAS package² of version from February 2008 in a similar manner to the HIRES and HDS procedures. The resolving power is $\sim 48\,000$ around 3300 \AA .

3. Stellar parameters

3.1. Effective temperatures

Many of our sample stars have been studied well in previous research (e.g., Chen et al. (2000); Reddy et al. (2003); Boesgaard & Novicki (2006); Tan et al. (2009); Boesgaard et al. (2011), but each uses a part of our entire sample. Directly mixing the stellar parameters from the literature will cause non-negligible biases because these authors adopted different approaches to deriving atmospheric parameters (T_{eff} , $\log g$, $[\text{Fe}/\text{H}]$, and ξ). For instance, Chen et al. (2000) and Reddy et al. (2003) both determined T_{eff} from the narrow-band photometric $b - y$ and c_1 given by Hauck & Mermilliod (1998) with the same color- T_{eff} relation (i.e., Alonso et al. 1996) and $\log g$ from the triangular parallaxes. While the T_{eff} and $\log g$ given by Boesgaard & Novicki (2006) were derived using excitation equilibrium of Fe I lines and an ionization balance between Fe I and Fe II.

Some research has shown systematic deviations between these two methods (e.g. Nissen 2013), and the reason can be attributed to the non-LTE effect of Fe I lines (e.g., Mashonkina et al. 2011; Korn et al. 2003). Recent study by Lind et al. (2012) has shown that the departures from LTE of Fe I lines result in underestimations by up to 0.4 dex of spectroscopic $\log g$ for metal-poor stars (see also Bensby et al. 2014). Considering many of our samples are nearby stars within 100 pc and therefore have precise HIPPARCOS parallaxes with relative uncertainties less than 10%, we determined the stellar parameters with the former approach.

For 28 stars that we share with Chen et al. (2000, 2001) or Reddy et al. (2003), we adopted the parameters determined by these studies, in which the narrow band photometric colors $b - y$ and c_1 from the uvby β catalog³ (Hauck & Mermilliod 1998) were used to derive T_{eff} with the calibration of Alonso et al. (1996), and $\log g$ were based on the HIPPARCOS parallaxes. A comparison of 23 common stars between Chen et al. (2000) and Reddy et al. (2003) shows excellent agreement in the stellar parameters between these two datasets, with the mean differences of only $8 \pm 41 \text{ K}$, $0.04 \pm 0.13 \text{ dex}$, and $-0.02 \pm 0.06 \text{ dex}$ on T_{eff} , $\log g$, and $[\text{Fe}/\text{H}]$, respectively.

To minimize the systematic bias, for stars not included in Chen et al. (2000) or Reddy et al. (2003), we preferably adopted the photometric colors $b - y$ and c_1 from Hauck & Mermilliod (1998) to derive their T_{eff} with the same calibration relation of Alonso et al. (1996). This made up another subset of 36 stars. For the remaining stars in our sample, broad-band colors $V - K$ were used to obtain T_{eff} with the calibration relation of Alonso et al. (1996). The V magnitudes were taken from the HIPPARCOS CATALOGUE, and K_s from the Two Micron All-Sky Survey (2MASS) were converted to K magnitudes in TCS system ac-

² <http://www.eso.org/sci/software/esomidass/>

³ <http://cdsarc.u-strasbg.fr/viz-bin/Cat?II/215>

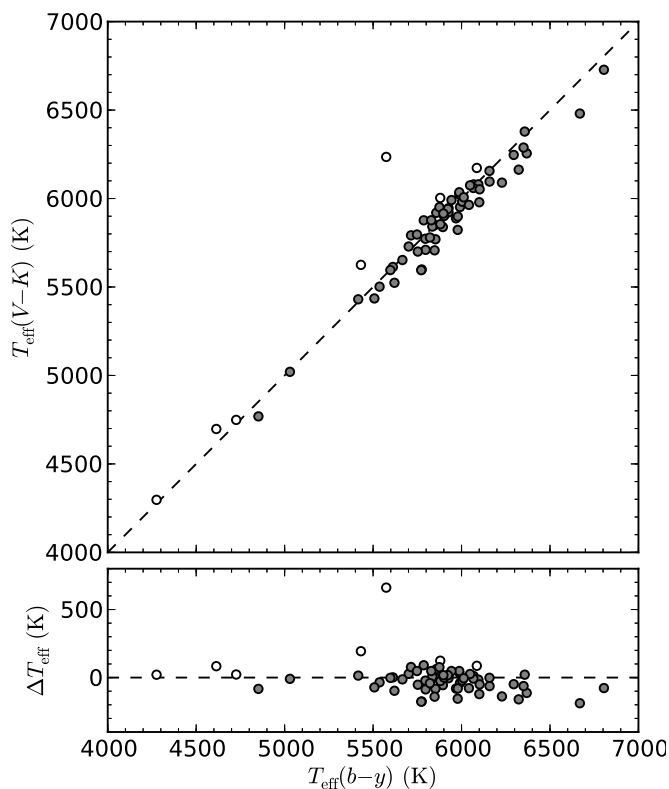


Fig. 1. Comparison of T_{eff} derived from the $b - y$ and $V - K$ colors for 66 stars. For stars with $d > 100$ pc (open circles), the reddening $E(V - K) = 2.72E(B - V)$ was taken into account (see text).

according to Ramírez & Meléndez (2004). Reddening due to interstellar extinction is only considered for stars with distances over 100 pc, and the values were interpolated from the dust map of Schlegel et al. (1998) based on COBE and IRAS satellites. Previous investigations (e.g., Arce & Goodman 1999) have shown that the $E(B - V)$ given by this map is slightly overestimated. We therefore reduced the values according to the formula given by Bonifacio et al. (2000) if $E(B - V) > 0.10$ and then further by a factor of $1 - \exp(-|D \sin b|/125)$, where D is the distance and b is the Galactic latitude of a given star.

Figure 1 compares the T_{eff} derived from $b - y$ and $V - K$ for 66 sample stars with the empirical calibration relations of Alonso et al. (1996). We found satisfactory agreement in the temperatures from these two colors. The mean difference $\langle T_{\text{eff}}(V - K) - T_{\text{eff}}(b - y) \rangle$ is -12 ± 112 K, and it drops to -22 ± 75 K after excluding the outlier HD 24289, which is probably affected by the large uncertainty ($\sim 37\%$) on its parallax distance and a relative high reddening value ($E(B - V) \approx 0.12$) toward this direction. The typical errors of $b - y$ (0.003) and c_1 (0.007) in Hauck & Mermilliod (1998) lead to the uncertainties of ~ 25 K for our sample stars, and the errors of 0.10 dex on $[Fe/H]$ translate into only 5 K on ΔT_{eff} . While for stars with T_{eff} derived with $V - K$, the typical uncertainties on the color indices and the transformations of K from 2MASS to TCS systems are around 0.036 and 0.035 mag, respectively. Therefore we estimated the T_{eff} uncertainties to be ~ 80 K, combining with the contributions of $\Delta[Fe/H] \approx 0.10$ dex. Although the difficulty estimating accurate interstellar reddening puts more uncertainties on T_{eff} , this is not the dominant factor for the majority of our samples.

3.2. Surface gravities

The surface gravities were determined from the fundamental equation

$$\log g = \log g_{\odot} + \log \left(\frac{M}{M_{\odot}} \right) + 4 \log \left(\frac{T_{\text{eff}}}{T_{\text{eff},\odot}} \right) + 0.4(M_{\text{bol}} - M_{\text{bol},\odot}) \quad (1)$$

where M denotes the stellar mass, and M_{bol} is the absolute bolometric magnitudes. We determined the masses by interpolating the Y^2 evolutionary tracks (Yi et al. 2003) with given metal content Z ($\approx 0.020 \times 10^{[Fe/H]}$) and by finding the track that passed through the corresponding points of the sample star on the (T_{eff}, L) plane. The HIPPARCOS parallaxes (van Leeuwen 2007) were essential for determining the absolute magnitude M_V and bolometric correction with the relation of Alonso et al. (1995). According to Formula 1, a relative 15% uncertainty for parallax will cause a $\log g$ uncertainty of 0.13 dex and will contribute most to the total error of the surface gravity. By considering the uncertainties on stellar masses and BC (see discussion in Tan et al. 2009), we estimated our $\log g$ uncertainties to be ± 0.15 dex. Considering that most of our sample stars have parallax uncertainties less than 10%, this is a conservative estimation.

However, this method is not feasible for ten of our sample stars without parallaxes. Alternatively, we adopted the surface gravities by forcing the Fe I and Fe II lines that give the same mean iron abundances. This was done for eight stars (G 10-4, G 21-22, G 24-25, G 88-10, G 113-22, G 126-36, G 130-65, and G 191-55), and their uncertainties were estimated by adjusting $\log g$ by an amount that led to an offset of $\Delta[Fe/H] = 0.1$ dex between the mean Fe I and Fe II abundances. The average Fe I abundance do not change significantly with the variations in $\log g$ within ± 0.2 dex, while the abundances derived from Fe II lines are more sensitive. We estimated the uncertainties of $\log g$ to be ≈ 0.18 dex for stars with surface gravities determined with the ionization balance method. There are fewer in subsample than in the total sample, so the errors of Pd or Ag abundances caused by the deviations of $\log g$ between the above two methods do not significantly bias our results.

3.3. Iron abundances and microturbulences

For the stars where we determined the parameters, the iron abundances $[Fe/H]$ were calculated by measuring the equivalent widths (W_{λ}) of ~ 20 selected Fe II lines, and the microturbulences (ξ) were determined by canceling out any trend in their individual abundances with the equivalent widths. The calibration relation of T_{eff} given by Alonso et al. (1996) is the function of both $[Fe/H]$ and color, therefore the determination of T_{eff} , $\log g$, $[Fe/H]$, and ξ is an iterative procedure. We searched the literature and took the $[Fe/H]$ values given by Boesgaard & Novicki (2006), Boesgaard et al. (2011), Simmerer et al. (2004), Gehren et al. (2006), Honda et al. (2006) and Ishigaki et al. (2012) as the initial values. We found the parameters converged to ΔT_{eff} within 3 K and $\Delta [Fe/H]$ within 0.01 dex after two to three iterations for most of our sample stars. The uncertainties of $[Fe/H]$ are estimated by changing the $\log g$ by ± 0.15 dex and combining the uncertainties of ~ 0.08 dex caused by the line-by-line scatter. In summary, the typical uncertainties for the temperatures, surface gravities, iron abundances, and microturbulence were estimated to 80 K, 0.15 dex, 0.10 dex, and 0.2 km s^{-1} , respectively.

3.4. Model atmospheres

We adopted the one-dimensional, line-blanketed, and local thermodynamic equilibrium MAFAGS-OS atmospheric model (Grupp 2004; Grupp et al. 2009) for sample stars and assumed that the mixing-length parameter $\alpha_{\text{CM}} = 0.82$, where the Canuto & Mazzitelli (1991, 1992) convection theory was used. The iron opacity was calculated based on the improved solar iron abundance of Lodders et al. (2009), and the opacities for metal-poor stars with $[\text{Fe}/\text{H}] < -0.6$ were calculated using α -element abundances enhanced by 0.4 dex.

3.5. Comparison with literatures

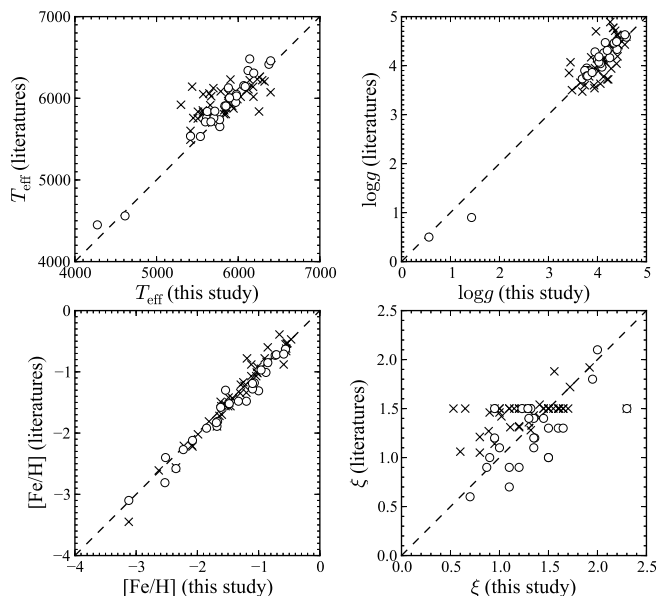


Fig. 2. Comparison of atmospheric parameters (T_{eff} , $\log g$, $[\text{Fe}/\text{H}]$ and ξ) of 25 common stars with Hansen et al. (2012) (*open circles*) and 44 common stars with Boesgaard et al. (2011) (*crosses*). There are eight overlapped stars in the above two subsamples. For the comparison with Boesgaard et al. (2011), the three stars with parameters taken directly from their work were not included.

Figure 2 compared the atmospheric parameters (T_{eff} , $\log g$, $[\text{Fe}/\text{H}]$ and ξ) of common stars with Hansen et al. (2012) and Boesgaard et al. (2011). Hansen et al. (2012) adopted a similar method to our study to determine the stellar parameters. For example, their T_{eff} were derived with $V-K$ and Alonso et al. (1996) relations and $\log g$ were based on HIPPARCOS parallaxes. The mean differences (Hansen et al. 2012 – this work) are $\langle \Delta T_{\text{eff}} \rangle = 89 \pm 99$ K, $\langle \Delta \log g \rangle = 0.04 \pm 0.16$, $\langle \Delta [\text{Fe}/\text{H}] \rangle = -0.09 \pm 0.12$, and $\langle \Delta \xi \rangle = -0.07 \pm 0.26$ km s $^{-1}$ for 25 common stars. Despite most of our parameters show good agreements with those of Hansen et al. (2012), temperatures, and/or iron abundances for a few stars differ up to >200 K and ~ 0.3 dex with theirs, which will cause non-negligible influences on Pd and Ag abundances. These include G 20-24 ($\Delta T_{\text{eff}} = 341$ K), HD 103723 ($\Delta T_{\text{eff}} = 248$ K), CD-30 18140 ($\Delta T_{\text{eff}} = 220$ K), HD 132475 ($\Delta T_{\text{eff}} = 217$ K), HD 111980 ($\Delta [\text{Fe}/\text{H}] = -0.31$ dex), and HD 106038 ($\Delta [\text{Fe}/\text{H}] = -0.28$ dex).

We also compared the parameters of 44 shared stars with Boesgaard et al. (2011) in Fig. 2. These authors derived their stellar parameters with the excitation equilibrium and ionization balance method. The mean differences (Boesgaard et al. 2011 –

this work) are $\langle \Delta T_{\text{eff}} \rangle = 129 \pm 211$ K, $\langle \Delta \log g \rangle = 0.04 \pm 0.28$, $\langle \Delta [\text{Fe}/\text{H}] \rangle = 0.00 \pm 0.13$, and $\langle \Delta \xi \rangle = 0.21 \pm 0.26$ km s $^{-1}$, which show larger scatters than those of Hansen et al. (2012). This is not surprising because the excitation equilibrium and ionization balance method relies on accurate Fe I abundances and is thought to be affected by non-LTE effects as mentioned above.

4. Stellar kinetics

We derived the Galactic motion velocities (U_{LSR} , V_{LSR} , W_{LSR})⁴ of the sample stars with the method given by Johnson & Soderblom (1987). The radial velocities of HDS and HIRES spectra were measured by finding the maximum of the cross-correlation functions with the high-resolution solar atlas (Kurucz 2005), and corrected to heliocentric velocities with the RVCORRECT task of the IRAF ASTUTIL package. The uncertainties of radial velocities were estimated by quadratically summing the drifts of ThAr line positions during an observing night, the R.M.S. of ThAr line centroid fitting, and the R.M.S. of measured radial velocities for every echelle order. The typical radial velocity uncertainties for HDS spectra are estimated to be around 0.5 km s $^{-1}$ and larger (~ 2 km s $^{-1}$) for HIRES spectra, which are dominated by larger drifts (~ 4 pixels) of ThAr lines in one night. For stars with UVES spectra, we adopted the values listed in the SIMBAD database directly. The parallax and proper motion data were taken from the new reduction of HIPPARCOS CATALOGUE (van Leeuwen 2007) or the TYCHO-2 CATALOGUE (Høg et al. 2000). For sample stars without HIPPARCOS parallaxes, we inverted Formula 1 with the spectroscopic T_{eff} and $\log g$ that were derived in Sect. 3, together with the basic relation $M_{\text{bol}} = V_{\text{mag}} + BC - 5 \log d + 5 - A_V$ to find their distances.

We adopted the solar motion of $(U, V, W)_{\odot} = (-10.00 \pm 0.36, +5.25 \pm 0.62, +7.17 \pm 0.38)$ km s $^{-1}$ (Dehnen & Binney 1998) to correct the (U, V, W) components of the sample stars to the local standard of rest (LSR). This allowed us to calculate the relative probabilities for the thick-disk-to-thin-disk (TD/D) and thick-disk-to-halo (TD/H) memberships of each star with the pure kinematic method proposed by Bensby et al. (2003). We emphasize that it is hard to clarify whether a star in the solar neighborhood belongs to the thin or the thick disk, and some other studies used chemical criteria such as $[\text{Fe}/\text{H}]$ and $[\alpha/\text{Fe}]$ (e.g., Fuhrmann 1998; Navarro et al. 2011). However, we simply divided our sample stars into three groups, thin disk, thick disk, and halo stars, according to whichever population had the highest probability based on the kinematic properties. We manually assigned four stars (HD 122563, HD 84937, HD 6268, and G 88-10) with $[\text{Fe}/\text{H}] < -1.5$ that are classified as thin disk stars by the kinetic method as halo stars. Previous studies have shown that all of them are enhanced in magnesium with $[\text{Mg}/\text{Fe}] > 0.49$ (e.g., Gratton et al. 2003; Honda et al. 2004; Boesgaard et al. 2011). Figure 3 shows the Toomre diagram of our sample stars, and the radial velocities, parallaxes, proper motions, and Galactic velocities are listed in the online Table 1.

5. Abundances

The ultraviolet Ag I λ 3280, 3382 Å, and Pd I λ 3404 Å regions are heavily blended by atomic and molecular lines. We used the spectral synthesis method with the IDL/Fortran SIU software package (Reetz 1991) to derive the Pd and Ag abundances of the sample stars. The relevant atomic data of Pd I and Ag I used

⁴ Here U is defined to be positive towards Galactic anticenter.

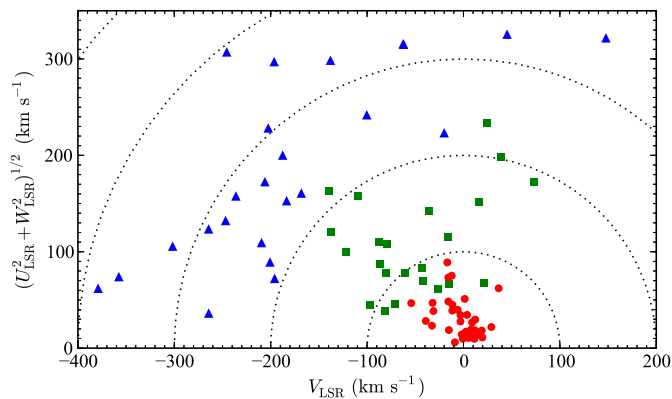


Fig. 3. Toomre diagram of sample stars in this work. Stars with the highest probability of belonging to the thin disk, the thick disk, and the halo are plotted with *red dots*, *green squares*, and *blue triangles*, respectively. Dotted lines represent total velocities of $|v|_{\text{LSR}} = \sqrt{U_{\text{LSR}}^2 + V_{\text{LSR}}^2 + W_{\text{LSR}}^2}$ in steps of 100 km s^{-1} .

in this work were presented in Table 3. For silver, the $\log gf$ values were taken from Ross & Aller (1972), where the hyperfine structure of both lines were taken into account. The $\log gf$ value of palladium was taken from the VALD⁵ database.

The overall $\log gf$ values for Ag I λ 3280.68 Å and λ 3382.90 Å are 0.005 and 0.002 dex higher than those of Hansen et al. (2012), respectively. While for Pd I, our adopted $\log gf$ is 0.02 dex lower. The van der Waals damping constants $\log C_6$ of both silver and palladium lines were calculated according to the Anstee & O'Mara (1991, 1995) interpolation tables. The blended atomic and molecular lines involve NH, Fe I, Fe II, Ni I, Ni II, V I, V II, Cr I, Ti I, and Ti II. We have considered the influence induced by the Zr II line on the red wing of Ag I λ 3280 Å by synthesizing the spectra with oscillation strength $\log gf = -1.1, -1.5$ (same as Hansen et al. 2012) and without this transition. We found that the differences are less than 0.03 dex for the deduced Ag abundance, and we did not include Zr II in our line list. The line information was taken from Kurucz database with slight adjustments. To minimize the systematic offsets and make a direct comparison with Hansen et al. (2012), we adopted the same solar abundance values ($\log \epsilon(\text{Ag})_{\odot} = 0.94$; $\log \epsilon(\text{Pd})_{\odot} = 1.57$) in our analysis as those used in their study.

Table 3. Atomic data

	λ (Å)	E_{low} (eV)	$\log gf$	$\log C_6$
Ag I	3280.682	0.00	-0.452	-31.795
Ag I	3280.683	0.00	-0.432	-31.795
Ag I	3280.688	0.00	-0.912	-31.795
Ag I	3280.690	0.00	-0.933	-31.795
Ag I	3382.899	0.00	-0.755	-31.829
Ag I	3382.900	0.00	-0.754	-31.829
Ag I	3382.905	0.00	-1.235	-31.829
Ag I	3382.908	0.00	-1.256	-31.829
Pd I	3404.582	0.81	0.300	-31.822

⁵ Vienna Atomic Lines Database, available at <http://vald.astro.univie.ac.at/vald/php/vald.php>

Figures 4, 5, 6 and 7 show the examples of spectral synthesis of the Ag I and Pd I lines for our sample stars. All of the four stars in Fig. 4 have solar metallicities or are mildly metal-poor, with $[\text{Fe}/\text{H}]$ ranging from -0.39 to $+0.05$. According to the kinetic criteria in section 4, they belong to the thin disk. Although the Ag I lines were heavily blended with Mn I (λ 3280.77 Å) or Fe I (λ 3382.98 Å), the spectral region can be well fitted by assuming Gaussian instrumental profiles.

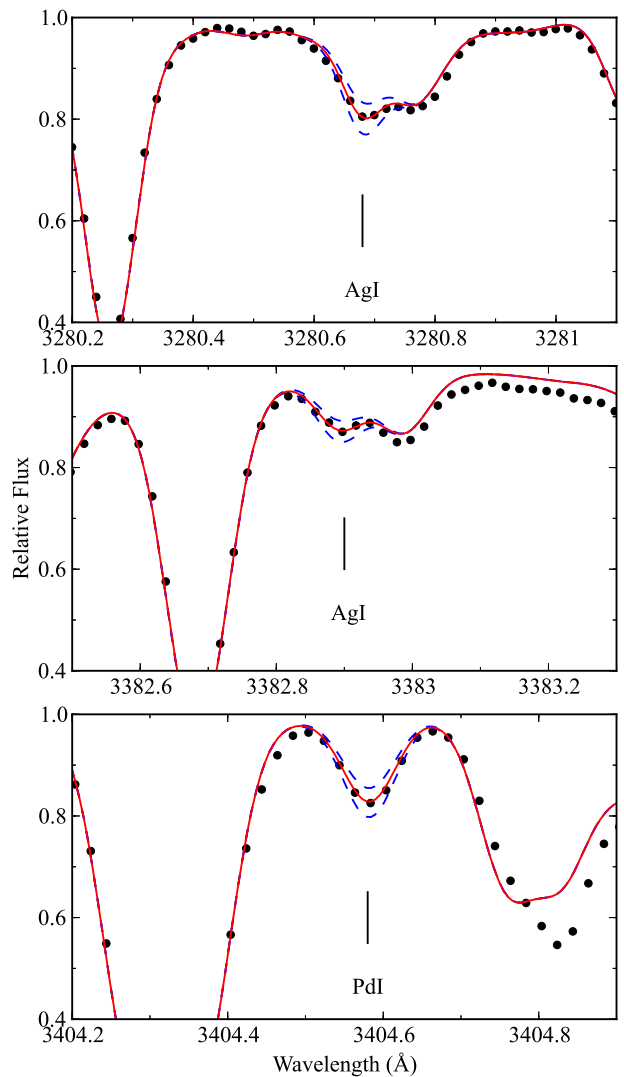


Fig. 6. Example of spectral synthesis around Ag and Pd regions used in this analysis. The dotted lines and red solid lines represent the observed spectra and synthesis spectra of HD 76932 ($[\text{Fe}/\text{H}] = -0.96$), respectively. The blue solid lines represent the synthesis spectra with $[\text{X}/\text{Fe}] \pm 0.1$ dex.

5.1. Error estimation

The errors in the derived chemical abundances are mainly due to the uncertainties in the stellar parameters and the continuum placement. Considering that the S/Ns of most spectra are higher than 100, the estimated abundance uncertainties caused by continuum location are around 0.15 dex. The errors caused by the uncertainties in the stellar atmospheric parameters are about 0.12 dex for Pd and 0.13 dex for Ag. Table 4 gives the abundance differences due to deviations of the effective temperature

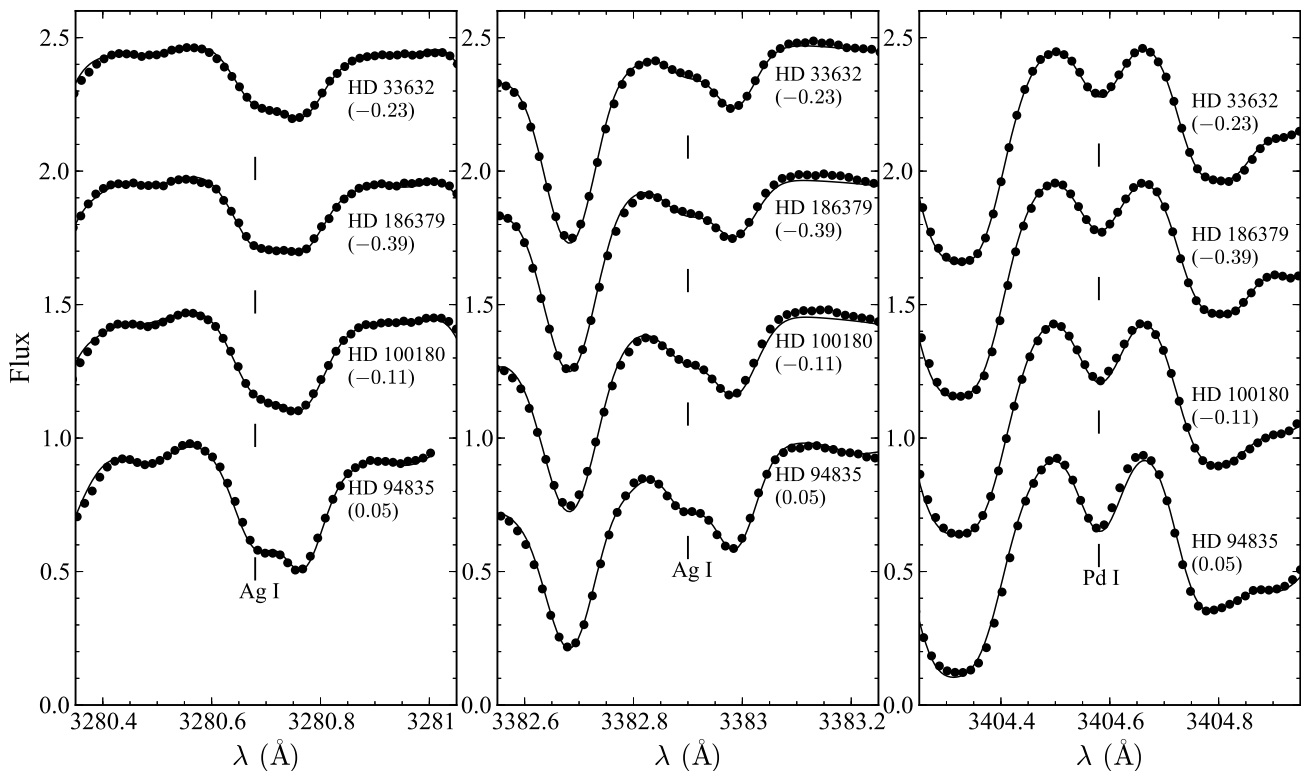


Fig. 4. Spectral synthesis for four thin disk stars in our sample. From top to bottom: HD 33632, HD 186379, HD 100180, and HD 94835. Solid dots represent the observed spectra with Keck/HIRES, and the solid lines are the synthesis spectra. Vertical lines indicate the location of Ag I and Pd I lines. Offsets of 0.5 were added from the bottom to the top to improve the visualization.

of 80 K, the surface gravity of 0.15 dex, the iron abundance of 0.10 dex and the microturbulent velocity of 0.2 km s^{-1} for a typical star, HD 76932. By quadratic summing of the above uncertainties, the errors of Pd and Ag abundances are estimated to be 0.19 and 0.20 dex, respectively.

5.2. Comparison with the literature

Hansen & Primas (2011) and the follow-up study (Hansen et al. 2012) derived Pd and Ag abundances for 34 dwarfs and 23 giants, of which 23 dwarfs and 2 giants are also included in our sample. We compared our abundances with the results of Hansen et al. (2012) for common stars in Fig. 8. We found excellent agreement with the Hansen et al. (2012) results. The mean differences are $\langle \Delta[\text{Pd}/\text{H}] \rangle = +0.017 \pm 0.145$ dex and $\langle \Delta[\text{Ag}/\text{H}] \rangle = -0.054 \pm 0.135$ dex, and both of the scatters are within the errors.

For G 183-11 and HD 140283, Hansen et al. (2012) did not report any Ag abundance, while we gave the upper limits based on the shallow absorption features exhibit in the spectra. The poor S/Ns and difficulties with locating the continuum placement properly has prevented any accurate measurements on these lines. While for CD -30 18140, we gave Pd I abundance value based on a weak line, because the absorption feature has exceeded the 3σ level below the continuum so cannot be fully explained by spectral noise. Similar features were also found for BD +21 607 and BD +17 4708. For G 20-24, we derived an upper limit of Pd I, and yet it is inconsistent with Hansen et al. (2012) ($[\text{Pd}/\text{Fe}] = 0.77 \pm 0.27$). We attribute this conflict to the large differences in the parameters determined by Hansen et al. (2012) ($T_{\text{eff}} = 6482 \text{ K}$, $[\text{Fe}/\text{H}] = -1.90$ dex) and this work

(6141 K, -1.68 dex). Their spectral synthesis are plotted in the righthand panel of Fig. 7.

In addition, for HD 103723, HD 106038, and HD 113679, our Pd I abundances are below the 1σ lower limits of Hansen et al. (2012). This is mainly due to the relative large differences in T_{eff} and/or the deviations in $[\text{Fe}/\text{H}]$, as discussed in Sect. 3.5.

Another source of deviations in the Ag abundance may arise from the two-level hyperfine splitting data of Ross & Aller (1972) adopted by this work and the three levels by Hansen et al. (2012). We selected 12 stars that span a wide range of T_{eff} and metallicities, and derived their Ag abundances with the above two sets of hyperfine splitting data. We found that the differences are within 0.01 dex, so much smaller than the claimed uncertainties of Ag in any studies, so they can be neglected.

Peterson (2013) also analyzed a sample of 29 turnoff stars and determined Pd abundances for 14 of them. There are 16 stars shared with our sample. For seven stars (BD +17 4708, BD +21 607, BD +37 1458, G 188-22, HD 31128, HD 106038, HD 160617), they did not report Pd abundance, but we gave detections. We plotted the Pd I regions in figure 7. For the remaining nine stars, our Pd abundances agree with their values very closely, except for G 191-55 and G 192-43. For G 191-55, Peterson (2013) gave $[\text{Pd}/\text{Fe}] = 0.3$, while we found a lower value of 0.11 dex. The difference again results from the large deviations of stellar parameters, especially T_{eff} (6000 K in Peterson 2013; 5570 K in our work). For G 192-43 ($[\text{Fe}/\text{H}] \approx -1.4$), where Peterson (2013) detected $[\text{Pd}/\text{Fe}] = 0.2$, we found $[\text{Pd}/\text{Fe}] = 0.39$ using the Pd I line of the same Keck/HIRES spectra. The line profile of Pd I $\lambda 3404.5 \text{ \AA}$ exhibits a W-shape, as shown in figure 7. We found that the synthesis spectrum with $[\text{Pd}/\text{Fe}] = 0.2$ and

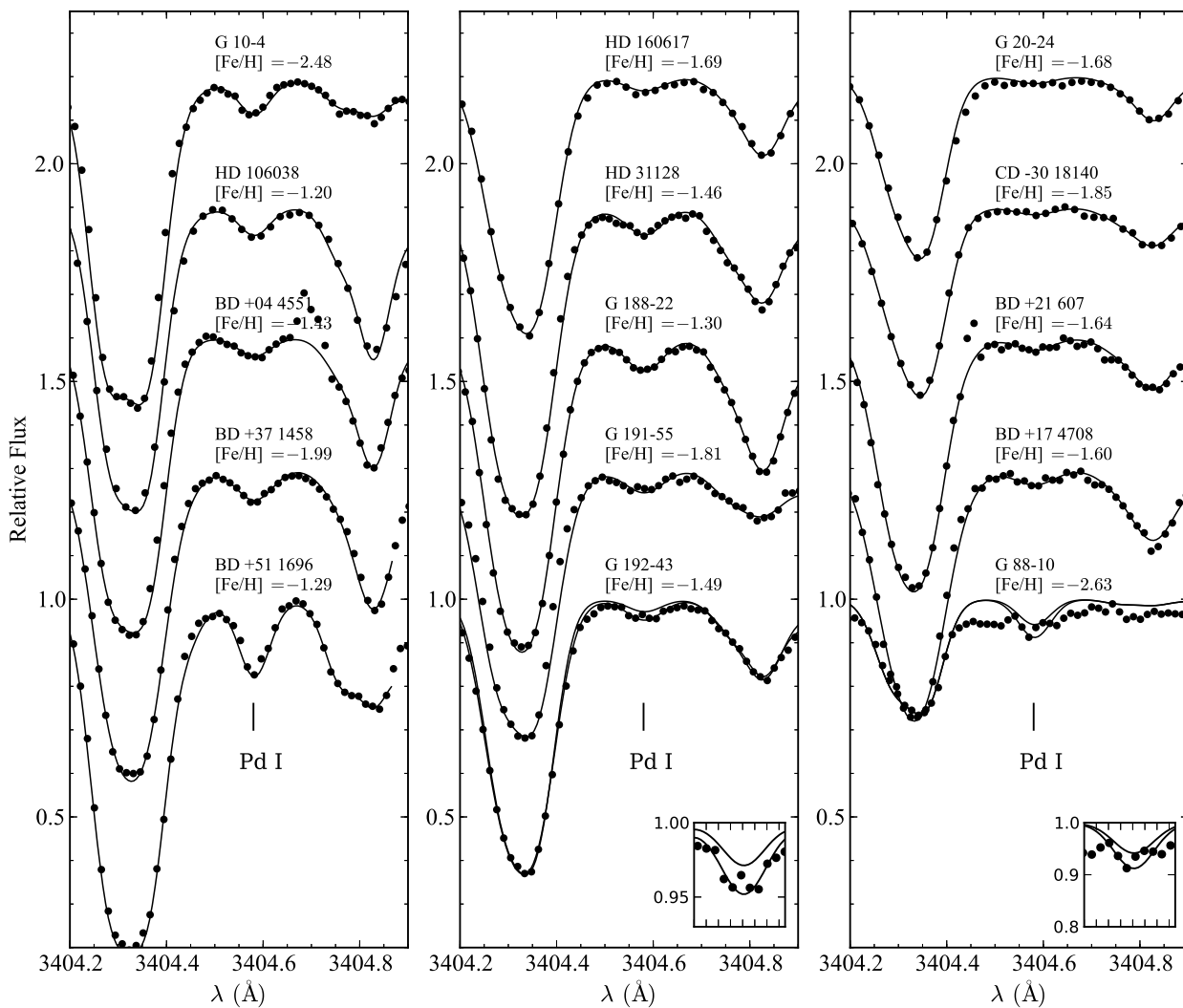


Fig. 7. Examples of spectral synthesis around Pd I $\lambda 3404.9\text{\AA}$ used in this analysis. The dots represent the observational data and solid lines the synthesis spectra. Offsets of 0.3 were added for better visualization. See also the online figure for details. For G 192-43, the absorption feature exhibits a W shape, as shown in the partial enlarged drawing of the spectrum in the lower right of the middle panel. Two synthesis spectra with $[\text{Pd}/\text{Fe}] = 0.20$ and 0.39 are overplotted, respectively. A similar plot was shown for G 88-10 (right panel), for which the lower synthesis ($[\text{Pd}/\text{Fe}] = 1.50$) was adopted as an upper limit.

Table 4. Abundance uncertainties of HD 76932, with $T_{\text{eff}} = 5849\text{ K}$, $\log g = 4.05$, $[\text{Fe}/\text{H}] = -0.96$, and $\xi = 1.6\text{ km s}^{-1}$.

Element ratios	$\Delta T_{\text{eff}} (\pm 80\text{ K})$	$\Delta \log g (\pm 0.15)$	$\Delta [\text{Fe}/\text{H}] (\pm 0.10)$	$\Delta \xi (\pm 0.2\text{ km s}^{-1})$	σ_{Total}
$[\text{Ag}/\text{H}]_{3382.9}$	± 0.10	∓ 0.01	± 0.06	± 0.01	± 0.11
$[\text{Ag}/\text{H}]_{3280.7}$	± 0.10	± 0.00	± 0.08	± 0.01	± 0.13
$[\text{Pd}/\text{H}]_{3404.6}$	± 0.10	± 0.01	± 0.07	± 0.01	± 0.12

their parameters ($T_{\text{eff}}/\log g/[\text{Fe}/\text{H}]/\xi = 6200/3.9/-1.5/1.2$) cannot explain the tip of the line core fully, whereas we have adopted the lower profile with slightly higher abundance.

6. Results and discussion

The resulting Pd and Ag abundances are listed in Table 2, which is only available online. For a few stars, we only get the upper or lower limits of abundance values because the lines are either too weak or are severely blended. The comparison of the Ag I abundances derived with the lines of $\lambda 3280\text{ \AA}$ and $\lambda 3382\text{ \AA}$ is shown in figure 9. The mean difference $\langle [\text{Ag}/\text{H}]_{3382} - [\text{Ag}/\text{H}]_{3280} \rangle$ is

-0.024 ± 0.068 dex, and there is no significant trend in the residual.

The abundance results of $[\text{Pd}/\text{Fe}]$ and $[\text{Ag}/\text{Fe}]$ versus $[\text{Fe}/\text{H}]$ are plotted in figure 10. The $[\text{Ag}/\text{Fe}]$ abundances are the averages of the values derived from the two Ag I lines, if neither of them are upper or lower limits. Otherwise only the values without limits are adopted. In general, $[\text{Pd}/\text{Fe}]$ and $[\text{Ag}/\text{Fe}]$ exhibit very similar behaviors with $[\text{Fe}/\text{H}]$. Both of them show flat trends above $[\text{Fe}/\text{H}] \gtrsim -0.6$, until solar metallicities up to $[\text{Fe}/\text{H}] \approx +0.1$, where the sample is dominated by thin disk stars. While the thick disk and halo stars are well mixed at $[\text{Fe}/\text{H}] < -1.0$, and both of the abundance ratios slowly increase with decreas-

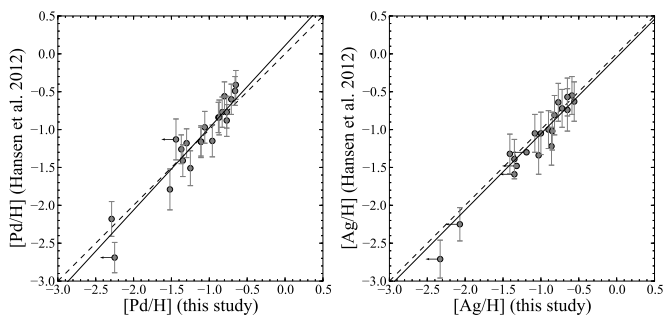


Fig. 8. Comparison of Ag and Pd abundances of common stars in this study with those in Hansen et al. (2012). The dashed lines represent 1:1 ratios, and solid lines represent the linear least-square fitting functions $y = (1.09 \pm 0.09)x + (0.11 \pm 0.10)$ for [Pd/H], and $y = (1.01 \pm 0.15)x + (-0.05 \pm 0.14)$ for [Ag/H], where x denotes our abundances and y denotes those of Hansen et al. (2012).

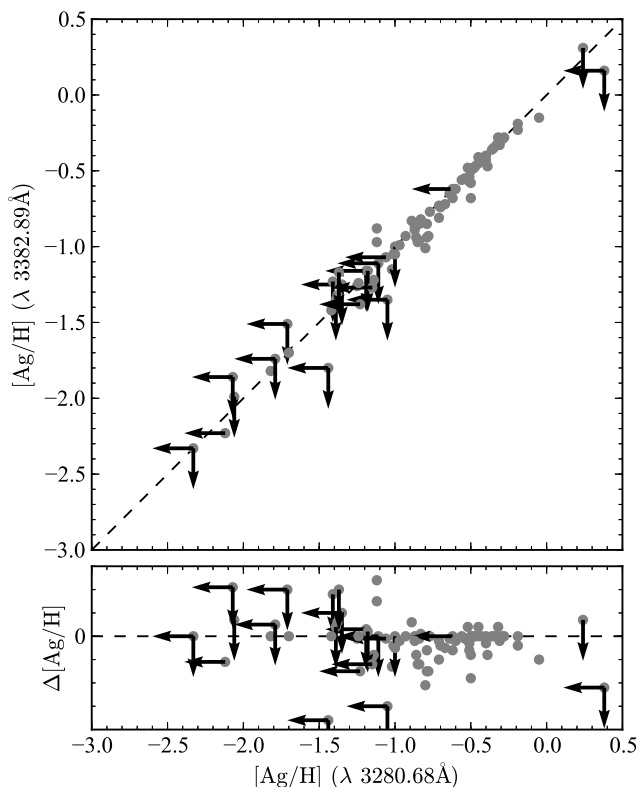


Fig. 9. Comparison of abundance values derived from Ag I $\lambda 3280.68 \text{ \AA}$ and Ag I $\lambda 3382.89 \text{ \AA}$. Arrows represent the upper or lower limits. The outlier with $x = -2.01$ and $y = -0.7$ is a spectroscopic binary G 88-10 (see discussions in section 6).

ing [Fe/H]. The large star-to-star scatters (0.16 dex for [Pd/Fe] and 0.30 dex for [Ag/Fe]) at [Fe/H] < -1.0 are not likely due to our internal errors but are probably caused by the inhomogeneous mixing of newly produced nuclides in the early Galaxy. And the descents of [Pd/Fe] and [Ag/Fe] with [Fe/H] at [Fe/H] ≈ -0.6 may be attributed to the rise of Fe in the SNIa yield.

We report the detections of Ag for a few metal-poor dwarfs with [Fe/H] ≤ -2.5 , although the number is small. For example, G 88-10 ([Fe/H] = -2.63) has an exceptional overabundance of [Ag/Fe] = +1.74, and the Pd abundance is likely to be overabundant as well ([Pd/Fe] < +1.50), as shown in Figs. 7 and 11. The enhancements of both Pd and Ag provide evidence of

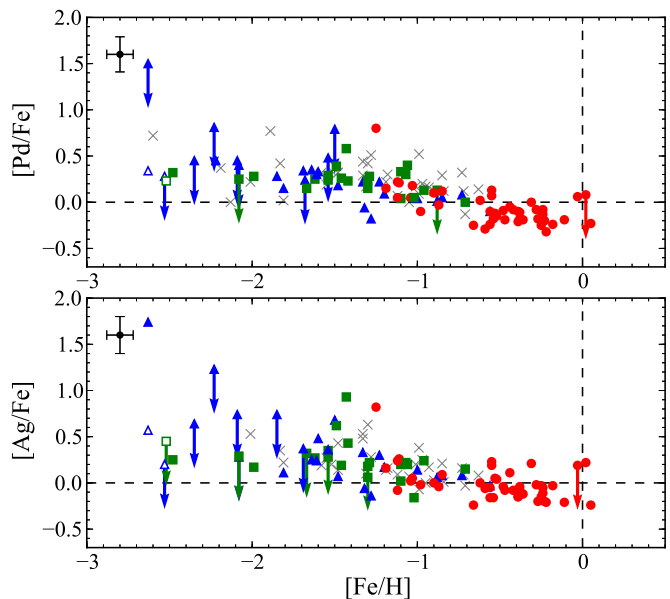


Fig. 10. [Pd/Fe] (upper panel) and [Ag/Fe] (lower panel) v.s. [Fe/H]. Red, green, and blue points represent thin disk, thick disk, and halo stars. Solid points denote dwarfs, while open circles denote the three giants in our sample. The arrows represent the lower or upper limits of the data points. The typical errors (see section 5.1) are shown in the upper left corner of each panel. The dwarfs in Hansen et al. (2012) are also plotted as crosses in this figure.

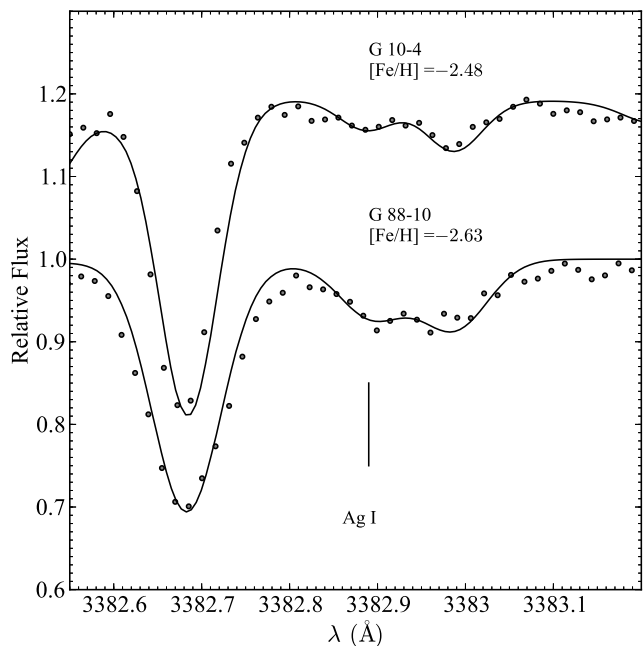


Fig. 11. Spectral synthesis of Ag I region for two stars, G 88-10 and G 10-4, at the metal-poor end in our sample. Both of them have metallicities of [Fe/H] ≈ -2.5 , and G 88-10 is a spectroscopic binary (see text).

a good correlation between these two elements, even in such a very metal-poor environment. Furthermore, G 88-10 is listed as a close binary system with $P = 20.6$ days in the SB9 catalog (Goldberg et al. 2002). Nevertheless, the overabundances of Ag and Pd (fairly high upper limit) are probably not due to the pho-

photospheric pollution via material transfer between the two companions, because this process is thought to be mainly responsible for the enhancements of s -process elements rather than r -process. Anyhow, the anomaly of G 88-10 deserves further investigations by connecting Pd and Ag with other elements produced by different nucleosynthesis processes, such as Ba and Eu. Another metal-poor star with $[\text{Fe}/\text{H}] \approx -2.5$ is G 10-4, for which we detected Pd I line at λ 3404.5 Å (figure 7) and Ag I line at λ 3382.9 Å (figure 11) based on Keck/HIRES spectra.

In figure 12 we plotted both the ratios of $[\text{Ag}/\text{H}]$ versus $[\text{Pd}/\text{H}]$ with colors coded by various Galactic populations. After excluding the three giants and the dwarfs with only upper or lower limits of Ag or Pd abundances, we found a least-square linear fitting of $[\text{Ag}/\text{H}] = (1.07 \pm 0.03) [\text{Pd}/\text{H}] + (0.09 \pm 0.03)$ for the entire sample. This is in general consistent with the slope of 0.97 by accounting for the uncertainties for the sample of dwarf + giant stars found by Hansen & Primas (2011). Furthermore, we found that the slope of Ag v.s. Pd stays constant at a wide abundance ratio range of $-2.2 \lesssim [\text{Pd}/\text{H}] \lesssim 0.1$ in the Galactic dwarfs. The mixing thick disk + halo stars almost show the same trend as that of thin disk stars. If the thick disk and halo stars are separated, the linear fits in figure 12 becomes $y = (1.05 \pm 0.10)x + (0.05 \pm 0.12)$ (thick disk) and $y = (1.09 \pm 0.07)x + (0.13 \pm 0.08)$ (halo), respectively.

It is well-known that the chemical evolution were dominated by the r -process in the early Galaxy. As the Galactic metallicity increases, the contribution of the s -process becomes significant because the time scales of low-mass AGB stars are considered to be much longer than that of the r -process (e.g., Burris et al. 2000). Arlandini et al. (1999) predicted that 46% of Pd and 20% of Ag in the solar system are produced by the s -process, and Bisterzo et al. (2011) got similar results (53.1% for Pd and 22.1% for Ag). Both of the calculations led to a slope of $[\text{Ag}/\text{H}]$ versus $[\text{Pd}/\text{H}]$ less than unity above $[\text{Fe}/\text{H}] \approx -1$ because the s -process produces roughly the same amount of Pd as does the r -process, but this fraction is only 1/5 for Ag. However, our results do not confirm the predictions of these stellar nucleosynthesis models. The trends in Ag vs. Pd in the Galactic dwarfs stay constant from a very metal-poor environment of -2.6 until the solar metallicity.

7. Conclusions

Based on the archive near-UV spectra obtained with Keck/HIRES, Subaru/HDS, and VLT/UVES, we analyzed a large sample of stars spanning the metallicity range of $-2.6 \lesssim [\text{Fe}/\text{H}] \lesssim +0.1$. We reported the photospheric abundances of palladium (Pd) and silver (Ag) for 83 and 79 stars, respectively, including several dwarfs with $[\text{Fe}/\text{H}] < -2.0$, which have seldom been detected in previous studies. The most metal-depleted dwarf with detected Ag abundance is down to $[\text{Fe}/\text{H}] \approx -2.6$. Meanwhile, our study investigated these two elements for the first time for a group of stars with solar and super-solar metallicities.

Our sample has increased the number of dwarfs with known Pd and Ag abundances by a factor of ~ 2 . It was found that both $[\text{Pd}/\text{Fe}]$ and $[\text{Ag}/\text{Fe}]$ show flat trends with metallicities around $-0.6 \lesssim [\text{Fe}/\text{H}] \lesssim +0.1$ and slowly increase with decreasing metallicity below $[\text{Fe}/\text{H}] \approx -0.6$. In metal-poor stars with $[\text{Fe}/\text{H}] < -1.5$, $[\text{Pd}/\text{Fe}]$ and $[\text{Ag}/\text{Fe}]$ ratios are enhanced by ~ 0.3 dex, and they show large star-to-star dispersions of ~ 0.3 dex. On the other hand, the amount of Pd in the Galactic dwarfs grows at nearly the same speed as does Ag at the whole $[\text{Pd}/\text{H}]$ ranging

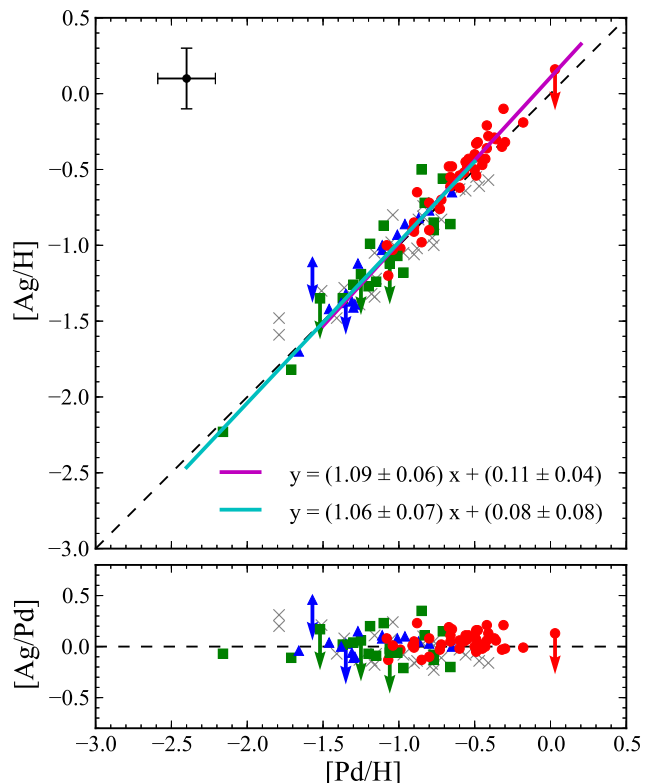


Fig. 12. Relation of $[\text{Ag}/\text{H}]$ versus $[\text{Pd}/\text{H}]$ (upper panel) and $[\text{Ag}/\text{Pd}]$ versus $[\text{Pd}/\text{H}]$ (lower panel) for the dwarfs in our sample. Red, green, and blue dots denote the sample stars that classified as thin disk, thick disk, and halo components by their kinetic properties, respectively (see section 4). The dashed line represents the 1:1 ratio, and the solid lines are the least-square linear fitting of the two subsamples of dwarfs (magenta: for thin disk stars; cyan: for thick disk + halo stars). The dwarfs in Hansen et al. (2012) are overplotted as crosses in this plot. The typical errors of Pd and Ag abundances are also shown in the upper left corner.

from -2.2 to -0.2 , and good correlations between $[\text{Ag}/\text{H}]$ and $[\text{Pd}/\text{H}]$ were found for different stellar populations. It seems that the trends in $[\text{Ag}/\text{H}]$ v.s. $[\text{Pd}/\text{H}]$ are the same within their errors for thin disk, thick disk, and halo stars. These facts imply that the two elements are synthesized by similar processes during the Galactic chemical evolution history, and our results do not support the theoretical predictions that Pd and Ag have different contributions from the s -process.

Acknowledgements. This research is supported by the National Natural Science Foundation of China under grant Nos. 11321064, 11233004, 11473033, and U1331122. The data used in this research were obtained from the Keck Observatory Archive (KOA), the Subaru-Mitaka-Okayama-Kiso Archive (SMOKA), and the ESO Science Archive Facility. KOA is operated by the W. M. Keck Observatory and the NASA Exoplanet Science Institute (NExSci), under contract with the National Aeronautics and Space Administration. SMOKA is operated by the Astronomy Data Center, National Astronomical Observatory of Japan. The observations of Keck/HIRES spectra were made under program ID H41aH, H11aH, H03aH, H177Hb, H269Hb, and H233Hb (P.I. A.Boesgaard). The observations of Subaru/HDS spectra were made under program ID o01319, o03310 (P.I. A.Boesgaard), o03429 (P.I. S.Honda), and o07136 (P.I. S.Wanajo). The observations of VLT/UVES spectra were done under program IDs 65.L-0507 and 67.D-0439 (P.I. F.Primas). We thank all the above P.I.s for obtaining the data that made this study possible. We thank the anonymous referee for the essential suggestions that improved this article. X.S.Wu thanks Dr. Kefeng Tan for providing the reduced UVES 1-D spectra. This research made use of the SIMBAD database, which is operated at the CDS, Strasbourg, France, and the data products from the Two Micron All Sky Survey, which is a joint project of the University of Massachusetts and the Infrared Processing and Analysis Center/California

Institute of Technology, funded by the National Aeronautics and Space Administration and the National Science Foundation.

References

- Alonso, A., Arribas, S., & Martínez-Roger, C. 1995, *A&A*, 297, 197
- Alonso, A., Arribas, S., & Martínez-Roger, C. 1996, *A&A*, 313, 873
- Anstee, S. D. & O'Mara, B. J. 1991, *MNRAS*, 253, 549
- Anstee, S. D. & O'Mara, B. J. 1995, *MNRAS*, 276, 859
- Arce, H. G. & Goodman, A. A. 1999, *ApJ*, 512, L135
- Arcones, A. & Montes, F. 2011, *ApJ*, 731, 5
- Argast, D., Samland, M., Thielemann, F.-K., & Qian, Y.-Z. 2004, *A&A*, 416, 997
- Arlandini, C., Käppeler, F., Wisshak, K., et al. 1999, *ApJ*, 525, 886
- Arnould, M. & Goriely, S. 2003, *Phys. Rep.*, 384, 1
- Bagnulo, S., Jehin, E., Ledoux, C., et al. 2003, *The Messenger*, 114, 10
- Bensby, T., Feltzing, S., & Lundström, I. 2003, *A&A*, 410, 527
- Bensby, T., Feltzing, S., & Oey, M. S. 2014, *A&A*, 562, A71
- Bisterzo, S., Gallino, R., Straniero, O., Cristallo, S., & Käppeler, F. 2010, *MNRAS*, 404, 1529
- Bisterzo, S., Gallino, R., Straniero, O., Cristallo, S., & Käppeler, F. 2011, *MNRAS*, 418, 284
- Boesgaard, A. M. & Novicki, M. C. 2006, *ApJ*, 641, 1122
- Boesgaard, A. M., Rich, J. A., Levesque, E. M., & Bowler, B. P. 2011, *ApJ*, 743, 140
- Bonifacio, P., Monai, S., & Beers, T. C. 2000, *AJ*, 120, 2065
- Burbidge, E. M., Burbidge, G. R., Fowler, W. A., & Hoyle, F. 1957, *Reviews of Modern Physics*, 29, 547
- Burris, D. L., Pilachowski, C. A., Armandroff, T. E., et al. 2000, *ApJ*, 544, 302
- Busso, M., Gallino, R., & Wasserburg, G. J. 1999, *ARA&A*, 37, 239
- Cameron, A. G. W. 1957, *PASP*, 69, 201
- Cameron, A. G. W. 2001, *ApJ*, 562, 456
- Canuto, V. M. & Mazzitelli, I. 1991, *ApJ*, 370, 295
- Canuto, V. M. & Mazzitelli, I. 1992, *ApJ*, 389, 724
- Chen, Y. Q., Nissen, P. E., Benoni, T., & Zhao, G. 2001, *A&A*, 371, 943
- Chen, Y. Q., Nissen, P. E., Zhao, G., Zhang, H. W., & Benoni, T. 2000, *A&AS*, 141, 491
- Clayton, D. D. & Rassbach, M. E. 1967, *ApJ*, 148, 69
- Crawford, J. L., Sneden, C., King, J. R., Boesgaard, A. M., & Deliyannis, C. P. 1998, *AJ*, 116, 2489
- Cristallo, S., Straniero, O., Gallino, R., et al. 2009, *ApJ*, 696, 797
- Dehnen, W. & Binney, J. J. 1998, *MNRAS*, 298, 387
- Dekker, H., D'Odorico, S., Kaufer, A., Delabre, B., & Kotzlowski, H. 2000, in *Society of Photo-Optical Instrumentation Engineers (SPIE) Conference Series*, Vol. 4008, *Society of Photo-Optical Instrumentation Engineers (SPIE) Conference Series*, ed. M. Iye & A. F. Moorwood, 534–545
- Farouqi, K., Kratz, K.-L., Mashonkina, L. I., et al. 2009, *ApJ*, 694, L49
- Farouqi, K., Kratz, K.-L., Pfeiffer, B., et al. 2010, *ApJ*, 712, 1359
- François, P., Depagne, E., Hill, V., et al. 2007, *A&A*, 476, 935
- Freiburghaus, C., Rosswog, S., & Thielemann, F.-K. 1999, *ApJ*, 525, L121
- Frischknecht, U., Hirschi, R., & Thielemann, F.-K. 2012, *A&A*, 538, L2
- Fuhrmann, K. 1998, *A&A*, 338, 161
- Gallino, R., Arlandini, C., Busso, M., et al. 1998, *ApJ*, 497, 388
- Gehren, T., Shi, J. R., Zhang, H. W., Zhao, G., & Korn, A. J. 2006, *A&A*, 451, 1065
- Goldberg, D., Mazeh, T., Latham, D. W., et al. 2002, *AJ*, 124, 1132
- Goriely, S., Bauswein, A., & Janka, H.-T. 2011, *ApJ*, 738, L32
- Goriely, S., Demetriou, P., Janka, H.-T., Pearson, J. M., & Samyn, M. 2005, *Nuclear Physics A*, 758, 587
- Gratton, R. G., Carretta, E., Claudi, R., Lucatello, S., & Barbieri, M. 2003, *A&A*, 404, 187
- Grupp, F. 2004, *A&A*, 420, 289
- Grupp, F., Kurucz, R. L., & Tan, K. 2009, *A&A*, 503, 177
- Hansen, C. J. & Primas, F. 2011, *A&A*, 525, L5
- Hansen, C. J., Primas, F., Hartman, H., et al. 2012, *A&A*, 545, A31
- Hauck, B. & Mermilliod, M. 1998, *A&AS*, 129, 431
- Hill, V., Plez, B., Cayrel, R., et al. 2002, *A&A*, 387, 560
- Høg, E., Fabricius, C., Makarov, V. V., et al. 2000, *A&A*, 355, L27
- Honda, S., Aoki, W., Ishimaru, Y., Wanajo, S., & Ryan, S. G. 2006, *ApJ*, 643, 1180
- Honda, S., Aoki, W., Kajino, T., et al. 2004, *ApJ*, 607, 474
- Ishigaki, M. N., Chiba, M., & Aoki, W. 2012, *ApJ*, 753, 64
- Johnson, D. R. H. & Soderblom, D. R. 1987, *AJ*, 93, 864
- Johnson, J. A. & Bolte, M. 2002, *ApJ*, 579, 616
- Just, O., Bauswein, A., Pulpillo, R. A., Goriely, S., & Janka, H.-T. 2015, *MNRAS*, 448, 541
- Käppeler, F., Beer, H., & Wisshak, K. 1989, *Reports on Progress in Physics*, 52, 945
- Käppeler, F., Gallino, R., Bisterzo, S., & Aoki, W. 2011, *Reviews of Modern Physics*, 83, 157
- Karakas, A. I., van Raai, M. A., Lugaro, M., Sterling, N. C., & Dinerstein, H. L. 2009, *ApJ*, 690, 1130
- Korn, A. J., Shi, J., & Gehren, T. 2003, *A&A*, 407, 691
- Korobkin, O., Rosswog, S., Arcones, A., & Winteler, C. 2012, *MNRAS*, 426, 1940
- Kratz, K.-L., Farouqi, K., Pfeiffer, B., et al. 2007, *ApJ*, 662, 39
- Kurucz, R. L. 2005, *Memorie della Societa Astronomica Italiana Supplementi*, 8, 189
- Lind, K., Bergemann, M., & Asplund, M. 2012, *MNRAS*, 427, 50
- Lodders, K., Palme, H., & Gail, H.-P. 2009, *Landolt Börnstein*, 44
- Mashonkina, L., Gehren, T., Shi, J.-R., Korn, A. J., & Grupp, F. 2011, *A&A*, 528, A87
- McLaughlin, G. C. & Surman, R. 2005, *Nuclear Physics A*, 758, 189
- Montes, F., Beers, T. C., Cowan, J., et al. 2007, *ApJ*, 671, 1685
- Navarro, J. F., Abadi, M. G., Venn, K. A., Freeman, K. C., & Anguiano, B. 2011, *MNRAS*, 412, 1203
- Nissen, P. E. 2013, *A&A*, 552, A73
- Noguchi, K., Aoki, W., Kawanomoto, S., et al. 2002, *PASJ*, 54, 855
- Perego, A., Rosswog, S., Cabezon, R. M., et al. 2014, *MNRAS*, 443, 3134
- Peterson, R. C. 2013, *ApJ*, 768, L13
- Pignatari, M., Gallino, R., Heil, M., et al. 2010, *ApJ*, 710, 1557
- Pignatari, M., Hirschi, R., Wiescher, M., et al. 2013, *ApJ*, 762, 31
- Ramírez, I. & Meléndez, J. 2004, *ApJ*, 609, 417
- Reddy, B. E., Tomkin, J., Lambert, D. L., & Allende Prieto, C. 2003, *MNRAS*, 340, 304
- Reetz, J. K. 1991, *Diploma Thesis*, Universität München
- Ross, J. E. & Aller, L. H. 1972, *Sol. Phys.*, 25, 30
- Rosswog, S., Liebendörfer, M., Thielemann, F.-K., et al. 1999, *A&A*, 341, 499
- Schlegel, D. J., Finkbeiner, D. P., & Davis, M. 1998, *ApJ*, 500, 525
- Simmerer, J., Sneden, C., Cowan, J. J., et al. 2004, *ApJ*, 617, 1091
- Sneden, C., Cowan, J. J., & Gallino, R. 2008, *ARA&A*, 46, 241
- Sneden, C., Cowan, J. J., Lawler, J. E., et al. 2003, *ApJ*, 591, 936
- Straniero, O., Chieffi, A., Limongi, M., et al. 1997, *ApJ*, 478, 332
- Tan, K. F., Shi, J. R., & Zhao, G. 2009, *MNRAS*, 392, 205
- Travaglio, C., Gallino, R., Arnone, E., et al. 2004, *ApJ*, 601, 864
- Travaglio, C., Gallino, R., Busso, M., & Gratton, R. 2001, *ApJ*, 549, 346
- van Leeuwen, F. 2007, *A&A*, 474, 653
- Vogt, S. S., Allen, S. L., Bigelow, B. C., et al. 1994, in *Society of Photo-Optical Instrumentation Engineers (SPIE) Conference Series*, Vol. 2198, *Instrumentation in Astronomy VIII*, ed. D. L. Crawford & E. R. Craine, 362
- Wanajo, S. & Janka, H.-T. 2012, *ApJ*, 746, 180
- Wanajo, S., Tamamura, M., Itoh, N., et al. 2003, *ApJ*, 593, 968
- Wasserburg, G. J. & Qian, Y.-Z. 2000, *ApJ*, 529, L21
- Woosley, S. E., Hoffman, R. D., Timmes, F. X., Weaver, T. A., & Thielemann, F.-K. 1997, *Nuclear Physics A*, 621, 445
- Yi, S. K., Kim, Y.-C., & Demarque, P. 2003, *ApJS*, 144, 259
- Zhao, G. & Magain, P. 1990, *A&A*, 238, 242

Table 1. Kinetic properties and stellar populations. The sample stars are organized into three subcategories, UVES, HDS, and HIRES, based the instruments (see online Table 2).

Star	V_{helio} (km s^{-1})	π (mas)	$\mu(\alpha) \cos \delta$ (mas/yr)	$\mu(\delta)$ (mas/yr)	U_{LSR} (km s^{-1})	V_{LSR} (km s^{-1})	W_{LSR} (km s^{-1})	Population
CD-30 18140	16.8	7.16 ± 1.45	-60.68 ± 1.80	-319.04 ± 1.11	-71.50	-195.90	-11.20	halo
CD-57 1633	260.7	9.91 ± 0.88	-94.08 ± 0.89	689.02 ± 1.08	306.30	-245.60	-24.90	halo
G 13-9	57.9	4.87 ± 1.51	-278.13 ± 1.67	-228.08 ± 0.91	93.10	-264.40	-81.40	halo
G 20-24	34.4	5.29 ± 2.52	-187.66 ± 2.29	-233.10 ± 1.99	-160.30	-206.00	64.30	halo
G 183-11	-242.7	9.38 ± 3.43	-222.94 ± 2.31	-352.20 ± 2.45	-53.50	-379.00	-31.60	halo
HD 61421	-3.2	284.56 ± 1.26	-714.59 ± 2.06	-1036.80 ± 1.15	-12.60	6.97	6.43	thin
HD 76932	119.4	47.54 ± 0.31	244.14 ± 0.23	213.94 ± 0.15	37.70	-86.20	78.20	thick
HD 84937	-15.0	13.74 ± 0.78	373.05 ± 0.91	-774.38 ± 0.33	-18.14	11.93	-3.52	halo
HD 97320	53.2	18.36 ± 0.58	160.06 ± 0.61	-201.30 ± 0.54	-83.50	-16.80	-30.50	thin
HD 97916	61.1	8.95 ± 1.14	208.21 ± 0.99	-8.80 ± 0.96	-117.70	15.90	96.10	thick
HD 103723	168.3	5.84 ± 1.38	-234.34 ± 1.05	-56.82 ± 0.72	65.80	-200.70	60.50	halo
HD 106038	99.4	9.98 ± 1.57	-216.24 ± 1.48	-439.18 ± 1.02	-25.20	-264.30	26.20	halo
HD 111980	155.0	10.50 ± 1.26	299.64 ± 0.96	-794.83 ± 0.63	-277.90	-196.40	-105.50	halo
HD 113679	157.8	8.75 ± 1.38	-386.94 ± 1.23	-145.79 ± 0.74	105.80	-301.70	0.10	halo
HD 121004	245.3	16.70 ± 1.24	-483.51 ± 1.47	8.54 ± 0.83	-74.90	-246.80	109.20	halo
HD 122196	-26.4	10.46 ± 1.07	-453.33 ± 0.89	-81.62 ± 0.83	160.90	-139.40	23.50	thick
HD 122563	-26.6	4.22 ± 0.35	-189.86 ± 0.27	-69.67 ± 0.19	0.84	6.91	-17.04	halo
HD 126681	-45.6	21.04 ± 1.12	-70.59 ± 1.24	-311.72 ± 0.72	12.30	-42.20	-68.90	thick
HD 132475	176.5	10.23 ± 0.84	-558.49 ± 0.85	-500.37 ± 0.68	-47.00	-357.50	57.40	halo
HD 140283	-169.0	17.16 ± 0.68	-1114.93 ± 0.62	-304.36 ± 0.74	-30.00	147.80	-320.50	halo
HD 160617	100.4	9.09 ± 1.31	-61.77 ± 1.55	-395.70 ± 1.10	-68.20	-209.50	-85.70	halo
HD 166913	-48.6	15.80 ± 0.91	-260.62 ± 0.93	-125.75 ± 0.68	35.00	-43.30	75.40	thick
HD 175179	21.7	14.59 ± 1.29	-133.71 ± 1.43	-431.46 ± 1.11	-117.70	-137.30	-25.60	thick
HD 188510	-192.5	26.71 ± 1.08	-38.11 ± 1.03	287.81 ± 1.13	141.10	-109.40	71.60	thick
HD 189558	-12.9	15.39 ± 0.81	-308.37 ± 0.85	-365.10 ± 0.86	-85.90	-122.20	50.10	thick
HD 195633	-45.8	10.07 ± 0.84	73.75 ± 0.93	22.59 ± 0.82	48.30	-15.70	-3.50	thin
HD 205650	-105.5	18.14 ± 0.96	342.91 ± 0.93	-208.50 ± 0.55	106.40	-79.50	17.30	thick
HD 298986	198.2	6.61 ± 1.41	408.70 ± 1.28	4.58 ± 1.15	-250.10	-138.00	163.30	halo
G 21-22	60.1	...	-168.90 ± 1.50	-446.20 ± 1.50^a	-61.27	36.47	10.06	thin
HD 6268	40.5	0.75 ± 0.78	-30.74 ± 0.83	-35.10 ± 0.80	-9.03	3.70	-33.31	halo
HD 94028	66.1	21.11 ± 0.92	-262.06 ± 1.02	-456.84 ± 0.63	13.82	-15.17	65.43	thick
HD 110184	140.2	0.76 ± 0.84	-14.14 ± 0.74	-9.19 ± 0.55	-28.54	-36.00	139.90	thick
HD 198390	5.0	32.66 ± 0.41	52.94 ± 0.38	96.82 ± 0.23	-12.44	9.32	5.52	thin
HD 201891	-43.9	29.10 ± 0.64	-122.95 ± 0.50	-899.21 ± 0.39	6.18	-32.64	22.44	thin
HD 220242	7.1	14.30 ± 0.72	-94.67 ± 0.51	-85.17 ± 0.44	-9.07	11.23	3.36	thin
BD+04 4551	-117.4	1.61 ± 2.66	-8.52 ± 2.42	77.87 ± 1.38	56.30	-79.90	53.47	thick
BD+07 4841	-234.3	5.06 ± 2.51	284.87 ± 2.73	-102.20 ± 1.77	48.69	-168.21	153.37	halo
BD+17 4708	-286.3	8.21 ± 1.26	511.75 ± 1.34	59.91 ± 1.17	42.31	-236.09	152.09	halo
BD+19 1185	-190.8	16.81 ± 2.04	664.05 ± 2.02	-622.42 ± 1.20	-197.74	39.09	11.84	thick
BD+21 607	339.9	11.40 ± 1.22	426.35 ± 1.23	-301.49 ± 0.95	306.31	45.24	-110.73	halo
BD+22 396	-23.5	10.59 ± 1.33	55.79 ± 1.43	-359.31 ± 1.04	-28.02	-3.10	19.81	thin
BD+37 1458	242.8	6.46 ± 1.31	71.30 ± 1.36	-352.80 ± 0.76	228.55	24.11	48.54	thick
BD+51 1696	65.3	12.85 ± 1.33	-870.07 ± 1.08	-543.76 ± 0.89	14.61	21.41	65.55	thick
BD-01 306	28.1	15.87 ± 1.23	994.75 ± 1.37	-79.73 ± 1.02	4.80	9.23	-16.39	thin
BD-17 484	235.3	5.75 ± 1.56	400.23 ± 1.31	-57.65 ± 1.33	87.33	-19.99	-205.64	halo
G 10-4	63.7	15.69 ± 2.75	-567.16 ± 3.62	-509.01 ± 2.06	1.86	-26.16	61.33	thick
G 24-25	-311.9	...	141.60 ± 1.40	-144.30 ± 1.40^a	186.04	-202.55	132.43	halo
G 63-46	-25.5	8.62 ± 1.43	111.35 ± 1.39	-286.45 ± 1.08	-2.40	7.48	-17.07	thin
G 74-5	27.4	18.45 ± 1.24	289.75 ± 1.29	-265.67 ± 1.04	8.98	19.58	-6.61	thin
G 88-10	84.1	...	-18.47 ± 7.97	-254.93 ± 4.40	69.35	-12.15	28.94	halo
G 113-22	56.2	...	224.40 ± 0.90	-150.40 ± 0.90^a	28.75	-31.19	25.53	thin
G 126-36	-87.1	...	-103.50 ± 1.10	-241.00 ± 1.10^a	10.61	-70.81	44.40	thick
G 130-65	-270.1	...	57.00 ± 1.60	-249.10 ± 1.60^a	-97.86	-187.56	174.71	halo
G 153-21	-63.4	11.92 ± 1.69	-230.94 ± 1.94	42.10 ± 1.49	43.25	1.28	-27.15	thin
G 180-24	-151.4	8.41 ± 1.02	-194.65 ± 1.03	-365.60 ± 1.01	29.08	-87.48	-106.00	thick
G 188-22	-93.2	9.03 ± 1.68	-237.88 ± 1.42	-159.34 ± 1.33	5.78	-81.32	38.00	thick
G 191-55	-257.2	...	191.10 ± 2.90	-110.00 ± 2.90^a	-233.16	-100.33	-65.16	halo
G 192-43	190.5	4.45 ± 1.90	-8.05 ± 1.50	-476.62 ± 1.37	152.53	73.06	79.79	thick
HD 14877	33.4	12.76 ± 1.16	136.34 ± 1.25	5.70 ± 0.90	13.52	18.97	-12.26	thin
HD 22521	-37.4	24.78 ± 1.15	-196.14 ± 1.17	-132.69 ± 0.98	-42.85	-11.52	13.88	thin
HD 24289	129.1	4.74 ± 1.74	271.32 ± 1.98	6.84 ± 1.78	85.10	-16.18	-77.48	thick
HD 24421	-32.8	26.38 ± 0.54	-119.17 ± 0.73	108.36 ± 0.58	-38.17	-11.58	7.76	thin
HD 25173	34.8	18.53 ± 0.42	167.95 ± 0.29	-308.55 ± 0.42	13.46	28.94	17.30	thin
HD 26421	-65.4	13.32 ± 0.92	119.37 ± 1.00	100.70 ± 0.83	-70.95	-15.69	18.44	thin
HD 28620	21.3	22.96 ± 0.59	30.85 ± 0.53	-7.84 ± 0.37	10.34	10.95	4.39	thin

Table 1. Continued.

Star	V_{helio} (km s^{-1})	π (mas)	$\mu(\alpha) \cos \delta$ (mas/yr)	$\mu(\delta)$ (mas/yr)	U_{LSR} (km s^{-1})	V_{LSR} (km s^{-1})	W_{LSR} (km s^{-1})	Population
HD 30743	-2.8	29.58 ± 0.49	-120.83 ± 0.47	-172.32 ± 0.36	-12.07	6.52	8.72	thin
HD 31128	111.9	15.00 ± 1.13	165.55 ± 0.81	-27.75 ± 1.25	50.22	-60.85	-60.11	thick
HD 33632	-0.6	38.29 ± 0.55	-145.00 ± 0.50	-135.14 ± 0.27	-10.67	5.12	7.16	thin
HD 54717	3.6	20.75 ± 0.62	-112.06 ± 0.95	-8.52 ± 0.55	-6.57	4.99	8.28	thin
HD 63333	-10.2	23.21 ± 0.47	-123.32 ± 0.53	-21.93 ± 0.45	-19.01	7.87	3.15	thin
HD 68284	63.8	13.14 ± 0.88	-10.74 ± 1.13	51.46 ± 0.69	37.07	-32.05	28.81	thin
HD 80218	-12.0	24.60 ± 0.58	-132.60 ± 0.55	-134.26 ± 0.26	-17.77	10.12	-0.67	thin
HD 89125	38.5	43.85 ± 0.36	-414.15 ± 0.37	-97.66 ± 0.19	9.01	-6.09	38.71	thin
HD 91638	-4.2	28.69 ± 0.53	-0.82 ± 0.50	-161.07 ± 0.49	-11.01	8.11	4.14	thin
HD 91889	-5.4	39.88 ± 0.37	268.46 ± 0.30	-672.57 ± 0.29	-10.89	9.34	3.75	thin
HD 94835	9.6	20.32 ± 0.66	-151.24 ± 0.77	-215.57 ± 0.49	-6.61	2.53	15.79	thin
HD 100180	-3.8	42.87 ± 1.22	-329.26 ± 1.28	-190.01 ± 0.98	-10.63	6.52	3.63	thin
HD 104056	-21.8	13.64 ± 1.03	111.11 ± 0.91	-177.14 ± 0.63	-8.07	17.36	-10.87	thin
HD 109303	24.0	11.30 ± 0.76	-97.95 ± 0.61	-47.76 ± 0.51	-3.99	12.18	29.41	thin
HD 118244	-17.0	21.60 ± 0.79	-248.95 ± 0.91	128.71 ± 0.51	-6.76	4.66	-9.54	thin
HD 134439	310.2	34.65 ± 1.28	-997.47 ± 1.20	-3543.55 ± 1.03	-255.28	-62.10	184.85	halo
HD 134440	310.9	35.14 ± 1.48	-999.75 ± 1.29	-3542.60 ± 1.13	-255.91	-62.56	184.94	halo
HD 186379	-6.7	22.53 ± 0.60	86.96 ± 0.47	-270.98 ± 0.52	-6.71	-0.65	7.07	thin
HD 194598	-246.4	17.00 ± 0.83	117.25 ± 0.83	-551.20 ± 0.91	133.00	-183.50	75.55	halo
HD 200580	-6.2	19.27 ± 0.99	-273.99 ± 1.03	-371.70 ± 0.47	-6.72	0.80	10.06	thin
HD 202884	-0.2	23.92 ± 0.76	143.76 ± 0.90	-41.31 ± 0.56	-9.86	5.03	7.27	thin
HD 204712	-25.2	14.56 ± 0.66	-108.73 ± 0.75	-142.88 ± 0.44	-0.62	-15.13	18.74	thin
HD 209320	-49.6	14.18 ± 0.87	19.23 ± 0.79	15.35 ± 1.07	-2.17	-39.08	28.09	thin
HD 209858	-1.8	18.00 ± 0.76	37.80 ± 0.72	-193.41 ± 0.80	-9.84	3.57	7.80	thin
HD 215442	-7.3	13.75 ± 0.61	127.89 ± 0.44	75.28 ± 0.43	-11.67	-1.86	8.02	thin
HD 241253	-15.0	8.66 ± 1.77	269.46 ± 2.21	-70.08 ± 1.23	-23.69	8.96	12.33	thin
HD 247297	38.8	4.61 ± 1.44	64.07 ± 1.65	-189.15 ± 1.02	27.56	-3.10	2.16	thin
HD 345957	-115.0	10.42 ± 1.14	-171.60 ± 0.56	63.37 ± 0.68	41.53	-97.09	17.70	thick
Ross 390	80.9	7.10 ± 2.45	423.11 ± 1.74	-482.21 ± 1.61	44.55	-54.20	13.96	thin
Ross 797	22.6	3.02 ± 2.38	76.68 ± 1.78	-433.46 ± 1.91	6.00	-8.91	-0.40	thin

Notes. ^(a) Stars with distances derived with spectroscopic $\log g$, and proper motions were taken from the TYCHO-2 CATALOGUE (see section 4). For other stars, parallaxes and proper motions were taken from the new reduction of HIPPARCOS CATALOGUE (van Leeuwen 2007).

Table 2. Stellar parameters and Pd and Ag abundances

Star	Instrument	T_{eff} (K)	$\log g$	[Fe/H]	ξ (km s^{-1})	T_{eff} method	[Pd/Fe]	[Ag/Fe] (3280 Å)	[Ag/Fe] (3382 Å)	[Ag/Fe] mean
CD –30 18140 ^a	VLT/UVES	6120	4.00	–1.85	1.50	$V - K$	0.28	< 0.74	< 0.74	< 0.74
CD –57 1633	VLT/UVES	5836	4.13	–0.88	1.35	$V - K$	0.01	0.09	0.03	0.06
G 13-9	VLT/UVES	6376	3.78	–2.23	1.35	$V - K$	<0.81	< 1.23	...	< 1.23
G 20-24	VLT/UVES	6141	4.16	–1.68	0.95	$V - K$	<0.24
G 183-11	VLT/UVES	6190	4.09	–2.08	1.50	$V - K$	<0.40	< 0.64	< 0.28	< 0.28
HD 61421	VLT/UVES ^c	6668	3.88	–0.03	1.95	$b - y$	0.06	< 0.41	< 0.19	< 0.19
HD 76932	VLT/UVES	5849	4.05	–0.96	1.60	$b - y$	0.13	0.25	0.23	0.24
HD 84937	VLT/UVES ^c	6323	4.02	–2.09	1.70	$b - y$	<0.45	< 0.74	< 0.84	< 0.74
HD 97320	VLT/UVES	5991	4.14	–1.11	1.35	$b - y$	0.21	0.33	0.18	0.26
HD 97916	VLT/UVES	6445	4.16	–0.88	1.50	$b - y^l$	< 0.13
HD 103723	VLT/UVES	5880	3.95	–0.85	1.32	$b - y$	0.05	0.08	0.08	0.08
HD 106038	VLT/UVES	5969	4.40	–1.20	1.00	$b - y$	0.09	0.19	0.15	0.17
HD 111980	VLT/UVES	5775	3.80	–1.00	0.95	$b - y$	0.04	0.11	0.17	0.14
HD 113679	VLT/UVES	5612	4.06	–0.56	1.10	$b - y$	–0.10	0.06	–0.12	–0.03
HD 121004	VLT/UVES	5598	4.34	–0.73	1.10	$b - y$	0.08	0.11	0.05	0.08
HD 122196	VLT/UVES	5978	3.85	–1.67	1.36	$b - y$	0.15	< 0.62	< 0.32	< 0.32
HD 122563	VLT/UVES ^c	4614	1.43	–2.53	1.95	$b - y$	< 0.28	< 0.20	< 0.20	< 0.20
HD 126681	VLT/UVES	5537	4.59	–1.10	0.70	$b - y$	0.33	0.26	0.14	0.20
HD 132475	VLT/UVES	5621	3.74	–1.48	1.23	$b - y$	0.18	0.07	< 0.25	0.07
HD 140283	VLT/UVES	5772	3.69	–2.35	1.65	$b - y$	< 0.45	< 0.64	< 0.84	< 0.64
HD 160617	VLT/UVES	5979	3.78	–1.69	1.50	$b - y$	0.34	< 0.37	...	< 0.37
HD 166913	VLT/UVES	6068	4.03	–1.54	1.29	$b - y$	0.29	< 0.35	< 0.38	< 0.35
HD 175179	VLT/UVES	5701	4.25	–0.71	1.20	$b - y$	0.00	0.15	0.15	0.15
HD 188510	VLT/UVES	5416	4.56	–1.62	0.90	$b - y$	0.25	0.24	0.30	0.27
HD 189558	VLT/UVES	5666	3.80	–1.07	1.35	$b - y$	0.30	0.23	0.22	0.22
HD 195633	VLT/UVES	5894	3.89	–0.59	1.45	$b - y$	–0.29	–0.05	–0.06	–0.06
HD 205650	VLT/UVES	5714	4.39	–1.10	0.87	$b - y$	0.04	0.08	–0.05	0.02
HD 298986	VLT/UVES	6086	4.03	–1.33	1.30	$b - y$	0.22	0.33	< 0.33	0.33
G 21-22	Subaru/HDS	5657	4.46	–0.98	1.35	$V - K$	–0.10	–0.14	0.10	–0.02
HD 6268	Subaru/HDS	4726	1.14	–2.63	2.05	$b - y$	0.34	0.57	< 0.64	0.57
HD 94028	Subaru/HDS	5926	4.23	–1.54	1.50	$V - K$	0.24	0.29	0.28	0.28
HD 110184	Subaru/HDS	4275	0.56	–2.52	2.00	$b - y$	0.23	< 0.45	< 0.66	< 0.45
HD 198390	Subaru/HDS	6339	4.20	–0.31	1.92	$b - y^l$	0.00	0.26	0.16	0.21
HD 201891	Subaru/HDS	5827	4.43	–1.04	1.55	$b - y^l$	0.05	0.04	–0.01	0.02
HD 220242	Subaru/HDS	6804	4.00	0.02	2.50	$b - y$	< 0.08	0.22	< 0.29	0.22
BD +04 4551 ^b	Keck/HIRES	5990	3.85	–1.43	1.41	$V - K$	0.58	0.91	0.95	0.93
BD +07 4841	Keck/HIRES	6187	3.93	–1.50	1.65	$V - K$	< 0.79	0.67	0.68	0.68
BD +17 4708 ^a	Keck/HIRES	5938	3.94	–1.60	1.30	$V - K$	0.33	0.48	...	0.48
BD +19 1185	Keck/HIRES	5507	4.41	–1.02	1.00	$b - y$	0.05	–0.12	–0.20	–0.16
BD +21 607 ^a	Keck/HIRES	6100	4.10	–1.64	1.45	$b - y$	0.35	0.25	< 0.29	0.25
BD +22 396	Keck/HIRES	5571	4.26	–1.12	0.80	$V - K$	0.05	0.00	0.15	–0.08
BD +37 1458	Keck/HIRES	5414	3.42	–1.99	1.10	$V - K$	0.28	0.17	0.17	0.17
BD +51 1696	Keck/HIRES	5567	4.41	–1.29	0.65	$V - K$	0.28	< 0.23	0.22	0.22
BD –01 306	Keck/HIRES	5646	4.32	–0.90	1.20	$V - K$	0.10	0.04	–0.04	0.00
BD –17 484	Keck/HIRES	6125	4.06	–1.54	1.20	$V - K$	< 0.48	0.36	< 0.38	0.36
G 10-4	Keck/HIRES	4974	4.50	–2.48	1.49	$V - K$	0.32	< 0.36	0.25	0.25
G 24-25	Keck/HIRES	5505	3.69	–1.61	1.35	$V - K$	0.30	0.24	< 0.44	0.24
G 63-46	Keck/HIRES	5696	3.97	–0.85	1.00	$V - K$	0.12	0.14	0.04	0.09
G 74-5	Keck/HIRES	5669	4.32	–0.87	0.53	$V - K$	–0.03	0.02	–0.10	–0.04
G 88-10 ^b	Keck/HIRES	5877	4.00	–2.63	1.60	$V - K$	< 1.50	...	1.74	1.74
G 113-22	Keck/HIRES	5565	3.95	–1.03	1.10	$V - K$	0.18	0.06	0.04	0.05
G 126-36	Keck/HIRES	5500	4.50	–1.06	0.80	$V - K$	0.40	0.27	0.12	0.20
G 130-65	Keck/HIRES	6031	3.65	–2.22	1.41	$V - K$	0.45
G 153-21	Keck/HIRES	5435	4.44	–0.66	1.61	$V - K$	–0.25	–0.14	–0.35	–0.24
G 180-24	Keck/HIRES	5959	4.12	–1.42	1.20	$V - K$	0.23	0.43	...	0.43
G 188-22	Keck/HIRES	5896	4.22	–1.30	1.11	$V - K$	0.24	...	< 0.18	< 0.18
G 191-55	Keck/HIRES	5570	4.11	–1.81	0.60	$V - K$	0.15	0.11	0.11	0.11
G 192-43	Keck/HIRES	6181	3.83	–1.49	1.32	$V - K$	0.39	0.62	0.62	0.62
HD 14877	Keck/HIRES	5971	4.03	–0.42	1.57	$b - y^3$	–0.08	–0.08	–0.08	–0.08
HD 22521	Keck/HIRES	5783	3.96	–0.25	1.55	$b - y^3$	–0.25	–0.15	–0.15	–0.15
HD 24289	Keck/HIRES	5682	3.48	–2.08	1.20	$b - y$	< 0.25	< 0.29	< 0.34	< 0.29
HD 24421	Keck/HIRES	5987	4.14	–0.38	1.51	$b - y^3$	–0.18	–0.07	–0.07	–0.07
HD 25173	Keck/HIRES	5867	4.07	–0.62	1.79	$b - y^l$	0.02	< 0.00	0.00	0.00
HD 26421	Keck/HIRES	5737	3.98	–0.39	1.53	$b - y^3$	–0.10	–0.11	–0.19	–0.15
HD 28620	Keck/HIRES	6101	4.08	–0.52	1.58	$b - y^2$	–0.15	0.04	0.04	0.04

Table 2. Continued.

Star	Instrument	T_{eff} (K)	$\log g$	[Fe/H]	ξ (km s ⁻¹)	T_{eff} method	[Pd/Fe]	[Ag/Fe] (3280 Å)	[Ag/Fe] (3382 Å)	[Ag/Fe] mean
HD 30743	Keck/HIRES	6294	3.99	-0.55	1.56	$b - y$	0.07	0.24	0.22	0.23
HD 31128	Keck/HIRES	5857	4.28	-1.46	0.89	$b - y$	0.26	< 0.31	0.19	0.19
HD 33632	Keck/HIRES	5962	4.30	-0.23	1.56	$b - y^l$	-0.20	-0.16	-0.24	-0.20
HD 54717	Keck/HIRES	6350	4.26	-0.44	2.00	$b - y^l$	-0.05	0.11	0.11	0.11
HD 63333	Keck/HIRES	6054	4.25	-0.38	1.46	$b - y^3$	-0.11	-0.02	-0.05	-0.04
HD 68284	Keck/HIRES	5832	3.91	-0.56	1.60	$b - y^2$	-0.10	-0.04	-0.06	-0.05
HD 80218	Keck/HIRES	6091	4.19	-0.28	1.51	$b - y^3$	-0.08	-0.04	0.00	-0.02
HD 89125	Keck/HIRES	6038	4.25	-0.36	1.66	$b - y^l$	-0.19	-0.12	-0.12	-0.12
HD 91638	Keck/HIRES	6160	4.29	-0.25	1.47	$b - y^3$	-0.16	-0.03	-0.03	-0.03
HD 91889	Keck/HIRES	6020	4.15	-0.24	1.66	$b - y^l$	-0.13	-0.05	-0.05	-0.05
HD 94835	Keck/HIRES	5814	4.43	0.05	1.26	$b - y^3$	-0.23	-0.24	-0.24	-0.24
HD 100180	Keck/HIRES	5866	4.12	-0.11	1.87	$b - y^l$	-0.19	-0.21	-0.21	-0.21
HD 104056	Keck/HIRES	5786	4.23	-0.55	1.30	$b - y$	0.13	0.19	0.19	0.19
HD 109303	Keck/HIRES	5905	4.10	-0.47	1.50	$b - y^l$	-0.19	-0.07	-0.08	-0.08
HD 118244	Keck/HIRES	6234	4.13	-0.53	1.92	$b - y^l$	-0.12	0.05	0.05	0.05
HD 134439	Keck/HIRES	5029	4.87	-1.28	0.60	$b - y$	-0.18	-0.14	-0.14	-0.14
HD 134440	Keck/HIRES	4851	4.99	-1.32	1.20	$b - y$	-0.06	< 0.09	-0.06	-0.06
HD 186379	Keck/HIRES	5806	3.99	-0.39	1.54	$b - y^3$	-0.21	-0.12	-0.18	-0.15
HD 194598	Keck/HIRES	5943	4.12	-1.23	1.50	$b - y$	0.22	0.30	0.30	0.30
HD 200580	Keck/HIRES	5829	4.39	-0.54	1.72	$b - y^l$	-0.18	-0.13	-0.18	-0.16
HD 202884	Keck/HIRES	6141	4.36	-0.24	1.42	$b - y^3$	-0.08	-0.11	-0.11	-0.11
HD 204712	Keck/HIRES	5888	4.12	-0.48	1.49	$b - y^3$	-0.09	-0.03	-0.06	-0.04
HD 209320	Keck/HIRES	5994	4.14	-0.18	1.51	$b - y^3$	-0.24	-0.01	-0.05	-0.03
HD 209858	Keck/HIRES	5911	4.26	-0.27	1.40	$b - y^3$	-0.18	-0.20	-0.20	-0.20
HD 215442	Keck/HIRES	5872	3.80	-0.22	1.69	$b - y^3$	-0.32	-0.21	-0.21	-0.21
HD 241253	Keck/HIRES	5877	4.08	-1.12	1.02	$V - K$	0.22	0.25	0.23	0.24
HD 247297	Keck/HIRES	5449	3.45	-0.56	1.15	$b - y$	-0.24	-0.14	-0.18	-0.16
HD 345957	Keck/HIRES	5752	3.91	-1.30	1.04	$b - y$	0.15	0.06	0.06	0.06
Ross 390	Keck/HIRES	5299	4.36	-1.19	0.95	$V - K$	0.15	0.16	...	0.16
Ross 797	Keck/HIRES	6255	3.87	-1.25	0.80	$V - K$	0.80	0.80	0.84	0.82

Notes. $b - y$ and $V - K$ in the column of method indicate T_{eff} derived from $b - y$ and $V - K$, respectively.

⁽¹⁾ Stellar parameters taken from Chen et al. (2000). ⁽²⁾ Stellar parameters taken from Chen et al. (2001). ⁽³⁾ Stellar parameters taken from Reddy et al. (2003). ^(a) Stars with lower spectral S/N and therefore the abundances are more uncertain than the average. ^(b) Stars in known binary systems. ^(c) Spectra taken from the UVES-POP survey.

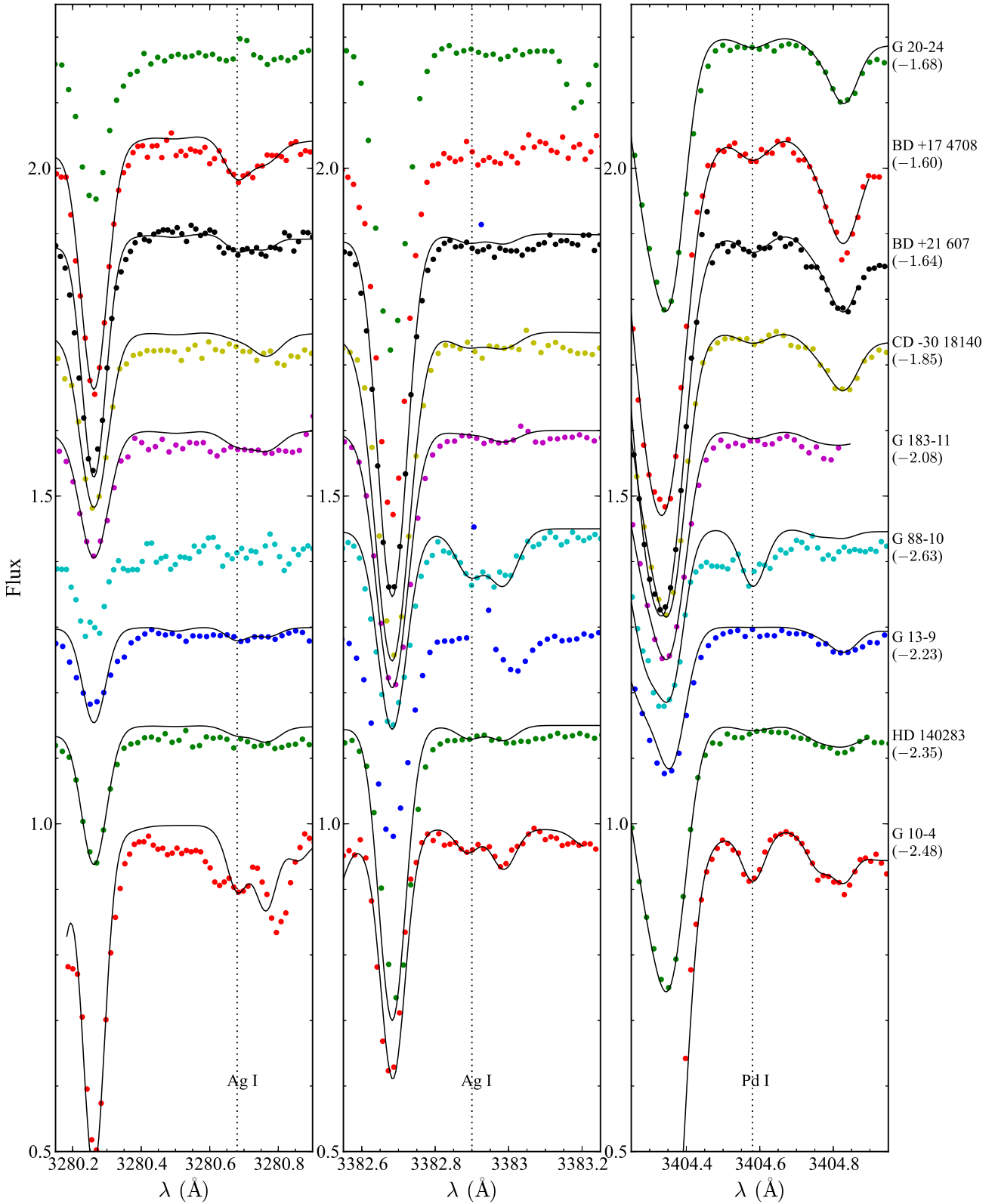


Fig. 5. Examples of spectral synthesis of metal-poor stars with $[\text{Fe}/\text{H}] < -1.5$. Colour dots and solid lines indicate observed and synthesized spectra, respectively. Vertical dash lines are the locations of Pd and Ag lines analyzed in this work. The $\text{Ag I } \lambda 3382.9 \text{ \AA}$ region of G 88-10 and the $\text{Ag I } \lambda 3382.9 \text{ \AA}$ regions of G 20-24 and BD +21 607 are severely affected by noise or do not show any absorption feature. The pixels in the $\text{Ag I } \lambda 3382.9 \text{ \AA}$ region of G 13-9 and $\text{Ag I } \lambda 3280.7 \text{ \AA}$ region of G 20-24 and BD +17 4708 were affected by cosmic rays, preventing us from any spectral synthesis. Ag abundance detections were obtained only for BD +17 4708 and BD +21 607 with $\text{Ag I } \lambda 3280.7 \text{ \AA}$ and only for G 88-10 and G 10-4 with $\text{Ag I } \lambda 3382.9 \text{ \AA}$ in this figure. Pd abundance detection were obtained for four stars with $\text{Pd I } \lambda 3404.6 \text{ \AA}$ (see online Table 2).